Heliyon

*Received:*
20 March 2018
*Revised:*
29 May 2018
*Accepted:*
13 July 2018

Cite as: D. Harinadha Reddy, Ananth Ramaswamy. Experimental and numerical modeling of creep in different types of concrete. Heliyon 4 (2018) e00698. doi: 10.1016/j.heliyon.2018.e00698

# Experimental and numerical modeling of creep in different types of concrete

**D. Harinadha Reddy, Ananth Ramaswamy** *

*Department of Civil Engineering, Indian Institute in Science, Bangalore, India*

* Corresponding author.
E-mail address: ananth@iisc.ac.in (A. Ramaswamy).

## Abstract

Creep in concrete, play a critical role in estimating losses in prestressed concrete structures, such as bridge girders, nuclear containment vessels, etc. The present study aims at investigating the creep under various environmental conditions in different types of concrete made with different ingredients using an experimental and numerical approach. Seven different concrete mixes have been made for this purpose and among the seven mixes, three mixes are self compacted concrete mixes (35 MPa, 55 MPa and 70 MPa), a high volume fly ash concrete mix (45 MPa), two mixes of normally vibrated ordinary Portland cement (OPC) concrete mixes (35 MPa and 45 MPa) and a heavy density concrete (25 MPa). Studies have been carried out at temperature of 25 °C and two relative humidity (RH) conditions (RH of 60% and 70%). An analytical model has been developed to simulate the drying phenomena in concrete based on a poromechanics approach. The hydration effects in blended cements (containing mineral admixture) is considered while developing the model. The proposed model is capable of predicting the degree of hydration, temperature and relative humidity (RH) over the continuum that required for estimating the creep strain. Micro prestress solidification (MPS) is used to estimate the creep strain. It is found that the proposed model is able to predict the drying phenomena and creep strain in various concretes, and which is in good agreement with the corresponding experimental results. It is found that heavy density concrete shows a higher creep strain than the other concretes. This may be due to the lower porosity of hematite aggregate. Further adding fly ash as a mineral admixture to concrete mix reduces the creep. Creep in a reinforced concrete (RCC) beam tested under sustained loading

https://doi.org/10.1016/j.heliyon.2018.e00698

and reported in the literature is simulated using the present model and it is seen that the model predictions are in good agreement with the test data.

Keywords: Structural engineering, Mechanical engineering, Materials science

## 1. Introduction

Prediction of delayed strains in concrete structures is crucial to assess its durability and serviceability conditions. These delayed strains can be classified as shrinkage and creep. The service life of a concrete structure depends on the curing conditions during the very early stage of the concrete's hardening process [1]. Cracks that appear at early ages may lead to an increased deterioration in the concrete thereby accelerating the corrosion of the embedded reinforcement by facilitating the pollutants and moisture. Damage so initiated that grows with time reduces the load carrying capacity of a structure. In order to enable an accurate prediction of the temperature field in hardening concrete elements, the evolution of the thermal characteristics of early age concrete is studied as a function of the state of the hardening process. The degree of hydration and moisture distribution are treated as fundamental parameters, and used for the description of the early age mechanical properties. Several models (Gawin et al. [2], Cervera et al. [3]) have been developed for predicting the degree of hydration and moisture distribution in concrete at early age.

Gawin et al. [2,4] proposed a numerical model to simulate concrete response at early ages and beyond. This model consider the concrete to be treated as a partially saturated porous material permitting the consideration of a hydration, evaporation–condensation, adsorption–desorption phenomena and nonlinearities due to temperature and pressure. According to this model the solid skeleton voids are filled with liquid water, water vapor and dry air. This model treated the dry air and water vapor phase through separate mass balance equations, Fourier equation to account for temperature balance and momentum balance equation is used to solve displacements. This study treated a fully coupled phenomena between each phase. This model is more sensitive to input parameters and also the model is more complicated and requires more computational power to solve the balance equations.

Using of high strength and high performance concrete is increasing rapidly in recent years. To achieve this high strength, many mineral admixtures (Fly ash, blast-furnace slag, silica fume etc.) are used in the concrete. Estimating time dependent deformations such as creep and shrinkage is very important for these newly developed concretes to its durability point of view. Ross [5] conducted creep tests on concretes containing fly ash. In these tests [5], the fly ash has replaced up to 25% of total OPC and this study reported that 15% reduction in creep when

compared to 100% OPC concrete. Bamforth [6] studied concretes containing fly ash and granulated furnace slag on various properties including creep. In this study, the concretes containing fly ash of 30% of total OPC showed 50% less creep strain than the concrete containing no fly ash. Lohtia et al. [7] studied creep behavior of fly ash blended concrete by replacing cement with fly ash from 0 to 25%. Unlike to Ross [5], this study shows an increase in creep for concretes containing more than 15% of fly ash than the normal concrete (without fly ash).

Buill and Acker [8] studied the creep properties of concretes where the part (25%) of the cement is replaced with silica fume as a mineral admixture. This study concluded that the silica fume containing specimen under drying conditions exhibited a lower creep than the controlled (no silica fume) specimen. Where as under sealed condition silica fume concrete showed a 12% higher creep than the controlled specimen.

Khatri and Sirivivatnanon [9] studied the creep properties of concrete mixes, where silica fume is mixed with other mineral admixtures, such as blast-furnace slag and fly ash. The mix containing 10% of silica fume showed a lesser creep than the controlled mix (no silica fume). Where as the mix containing 65% of blast-furnace slag and 10% of silica fume did not effect in creep strain when compared with the controlled mix (100% OPC concrete). This study [9] also indicated that creep strain in the mix containing fly ash of 15% or 25% with 10% silica fume is increased, when compared to the controlled mix. Mazloon et al. [10] studied the long term creep properties for concrete mixes containing silica fume (0, 6, 10, 12%), and shows that the creep strain decreased with increase in silica fume.

The studies came up with different conclusions on creep for concrete containing high volume fly ash (HVF). Some studies [5,6] shows that the increase in fly ash content increases creep where as some other authors [7,11] concluded that the increase in fly ash content decreases the creep. This needs a further investigation on creep for concretes containing high volume fly ash. Few authors [12,13,14] studied the creep effects in self compacted concrete (SCC) mixes containing mineral admixtures. No studies showed the effects of iron ore aggregate on creep strain in the concrete.

There are numerous reasons reported in the literature for differences in creep in various concretes. Unhydrated fly ash, particularly in high volume fly ash mix, serves as micro aggregates and restrains the creep deformation. Since, creep has been controlled by different mechanisms, in this study an attempt has been made to study the creep behavior of different types of concrete made with different ingredients. Firstly, a study is carried out by comparing two types of concrete such normal vibrated concrete and self compacting concrete. As self compacting concretes are made with more volume of paste, the problem of creep is predominant and it needs to be studied. Secondly, low volume fly ash concrete behaves differently than high volume fly ash concrete in developing creep properties due to the above mentioned

 https://doi.org/10.1016/j.heliyon.2018.e00698

**Table 1.** Chemical composition of cement, fly ash and silica fume [%].

| Compound | Cement | Fly ash | Silica fume |
|---|---|---|---|
| $CaO$ | 64.1 | 6.02 | – |
| $SiO_2$ | 21.0 | 62.63 | 95.60 |
| $Al_2O_3$ | 5.1 | 15.5 | – |
| $Fe_2O_3$ | 3.1 | 6.5 | – |
| $MgO$ | 2.5 | 3.0 | – |
| $SO_3$ | 2.2 | – | – |
| $K_2O$ | 0.7 | – | – |
| $Na_2O$ | 0.3 | – | – |
| Chloride | 0.03 | – | – |
| Insolubles | 0.3 | 2.0 | – |
| Loss on Ignition | 0.6 | 4.35 | 2.40 |
| Free lime | 0.80 | – | – |

reasons. Hence, the influence of volume of fly ash needs to be studied. Thirdly, aggregates have a significant role to play in controlling the creep properties. In view of this, two types of aggregates like conventional aggregate and hematite aggregates were used in this study. Overall, this study aims to investigate the influence of various ingredients on creep properties by conducting experiments. Further, a model to predict the creep behavior in various types of concrete by analytically has been developed and validated.

## 2. Experimental

### 2.1. Raw materials

The aggregates used in the concrete were siliceous aggregate (granite) as the coarse aggregate conforming to IS:383 (1970) [15]. The hematite ore aggregate used for the special concrete that has been used in the nuclear power plant structures. These aggregates were extracted from the hematite ore as a maximum size of 20 mm. River sand and crushed siliceous stone (quarry dust) conforming to IS:383 (1970) [15] was used as a fine aggregate in the concrete. The fine aggregates for heavy density concrete is also extracted from the hematite ore conforming to IS:383 (1970) [15]. Type III cement (grade 53) conforming to IS:12269 (1987) [16] was used in the mix design as a binding material. In addition to cement, Class F fly ash [17] and silica fume (micro silica) as mineral admixtures were used for the preparation of self compacted concrete and High volume fly ash concrete. A Polycarboxylic ether, a polymer based super-plasticiser [18] was used in the mix design as a high range water reducer for improving workability of concrete in fresh state. Potable water was used in all the mixes. The chemical composition of the cement, fly ash and silica fume are as shown in the Table 1.

**Table 2.** Concrete mix proportions given in values of kg/m$^3$ of concrete.

| | H25* | M35* | M45* | F45* | SCC35* | SCC55* | SCC70* |
|---|---|---|---|---|---|---|---|
| C | 350 | 350 | 385 | 300 | 490 | 480 | 498 |
| **CA (G)** | | | | | | | |
| 40 mm | 0 | 331 | 0 | 0 | 0 | 0 | 0 |
| 20 mm | 0 | 441 | 613 | 703 | 0 | 0 | 0 |
| 12 mm | 0 | 331 | 409 | 444 | 758 | 699 | 683 |
| **CA (IO)** | | | | | | | |
| 20 mm | 1116 | 0 | 0 | 0 | 0 | 0 | 0 |
| 12 mm | 704 | 0 | 0 | 0 | 0 | 0 | 0 |
| $FA_g$ | | | | | | | |
| NRS | 0 | 470 | 492 | 241 | 865 | 819 | 838 |
| CS (G) | 82 | 320 | 334 | 463 | 0 | 0 | 0 |
| IOS | 1340 | 0 | 0 | 0 | 0 | 0 | |
| w/c | 0.48 | 0.45 | 0.4 | 0.48 | 0.45 | 0.45 | 0.39 |
| w/b | 0.48 | 0.45 | 0.4 | 0.29 | 0.45 | 0.38 | 0.30 |
| FA | 0 | 0 | 0 | 200 | 0 | 96 | 98 |
| SF | 0 | 0 0 | | 0 | 0 | 0 | 49 |
| AD | 4.32 | 4.55 | 4.93 | 6.1 | 3.61 | 8.78 | 10.08 |

* Note: C is cement; CA(G) is coarse aggregate (Granite); CA(IO) is coarse aggregate (Iron ore); NRS is natural river sand; CS(G) is crushed sand (Granite); $FA_g$ is fine aggregate; IOS is iron ore sand; w/c is water to cement ratio; w/b is water to binder ratio; FA is fly ash; SF is silica fume and AD is admixture.

## 2.2. Mix details

Four different concretes, namely normal strength (M35, M45), heavy density (H25), self compacted (SCC35, SCC55 and SCC70) and high volume fly ash (F45) concrete with total 7 mixes were prepared to study the creep. The mix details is as shown in the Table 2.

In this study, the first alphabets of the mix denotes the type of concrete and is followed by the numeric value that represents its average compressive strength tested after 28 days from casting and cured under water. High volume fly ash concrete denoted by 'F', normal strength concrete represented by 'M' and self compacted concrete denoted as SCC, and heavy density concrete represented as 'H'. For example SCC35 represents, self compacted concrete and its average uniaxial compressive strength is 35 MPa. For SCC35 no mineral admixture is added, where as for SCC55, fly ash is added as a mineral admixture and for SCC70, both fly ash (class F) and silica fume (micro silica) were added as mineral admixture. For high volume fly ash concrete (F45), 40% of cement by weight was replaced with class 'F' fly ash. For Heavy density concrete, a hematite ore aggregate is used as coarse and fine aggregate.

## 2.3. Specimen preparation for creep

A standard cylinder specimen of 300 mm in height and 150 mm in diameter is used for measuring creep strain for all the 7 mixes specified in the Table 2. The

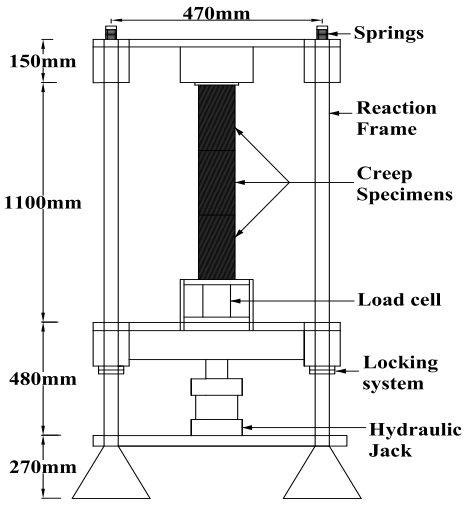


**Figure 1.** Schematic representation of test setup for creep.

cylinders were cast and immediately the surface was sealed using plastic wrap and placed in the walk-in humidity and temperature controlled chamber. At an age of 24 hours, the specimens were demolded. Sets of companion cubes were kept in the room under the same condition and tested under uniaxial compression to know the strength of the concrete at the time of testing the creep specimen. The top and bottom surfaces were sealed to prevent drying. However, the lateral surface were exposed to controlled temperature and humidity in the chamber and were undergoing gradual drying. These specimens were cured under different relative humidities of 60%, and 70% with constant temperatures of 25 °C in separate controlled chambers until the tests were completed. Further the specimens have been loaded at different ages to assess the influence of concrete age on creep in concrete.

The creep rig has been used for loading the concrete specimen as shown in Figures 1 and 2. Three specimens were placed one on top of the other in the creep frame for loading as per ASTM C512 [19]. Demec gauge pins were fixed on two pairs of two diametrically opposite faces of the cylinder with a standard gauge length (100 mm), so that an average strain across each specimen could be reckoned from periodic measurements at constant load. The loading was applied through a jack and the load level measured by a load cell as shown in Figure 1. Once the desired load level was reached, this was locked by using the locking nuts on each corner post of the frame. Different levels of loading (20% and 30% of $f_c$) was applied on these specimens. After application of desired load the instantaneous strain of the specimen was measured immediately by using Demec gauge (strain gauge used for measuring the strains between two Demec points and the least count of the gauge is 0.0000157 m). The strain measurements are taken at each day after jacking to ensure constant load is maintained till the completion of the test. Combinations of load levels for each mix and age at loading and RH have been tested in the present study.


https://doi.org/10.1016/j.heliyon.2018.e00698

**Figure 2.** Reaction frame for creep test.

**Table 3.** Shrinkage (in micro strains) data for all concretes, cured at 60% RH and 25 °C.

| | H25 | M35 | M45 | F45 | SCC35 | SCC55 | SCC70 |
|---|---|---|---|---|---|---|---|
| 7 days | 210 | 180 | 160 | 197 | 164 | 110 | 82 |
| 14 days | 458 | 320 | 300 | 245 | 345 | 161 | 135 |
| 28 days | 514 | 415 | 380 | 299 | 449 | 263 | 229 |
| 50 days | 590 | 461 | 440 | 376 | 475 | 321 | 290 |
| 75 days | 643 | 520 | 530 | 467 | 545 | 443 | 412 |
| 100 days | 665 | 555 | 540 | 515 | 571 | 445 | 431 |
| 114 days | 672 | 559 | 548 | 538 | 582 | 451 | 442 |
| 128 days | 681 | 562 | 560 | 540 | 591 | 457 | 448 |

The data has been reported by normalizing the compliance with respect to the applied load. The normalized total compliance was estimated by deducting the shrinkage strain measured from the companion prism specimens cured at similar conditions of the creep specimen. The water loss was also measured each time simultaneously by weighing the companion specimens and computed the change in weight. The shrinkage strains at different ages are presented in the Table 3 and 4. The water loss data for all the concretes measured at different ages are given in the Tables 5 and 6.

## 2.4. Experimental results

### *2.4.1. Compressive strength*

Compressive strength of companion concrete was measured using the standard cube of dimension 150 mm × 150 mm × 150 mm. Compressive strength measured at different levels of ages starting from 14 days, 28 days, 90 days, 180 days and 360 days

 https://doi.org/10.1016/j.heliyon.2018.e00698

**Table 4.** Shrinkage (in micro strains) data for all concretes, cured at 70% RH and 25 °C.

| | H25 | M35 | M45 | F45 | SCC35 | SCC55 | SCC70 |
|---|---|---|---|---|---|---|---|
| 7 days | 154 | 155 | 147 | 131 | 101 | 66 | 65 |
| 14 days | 384 | 280 | 260 | 158 | 210 | 110 | 103 |
| 28 days | 452 | 340 | 315 | 225 | 296 | 235 | 208 |
| 50 days | 545 | 410 | 360 | 310 | 375 | 333 | 298 |
| 75 days | 611 | 465 | 450 | 321 | 502 | 396 | 310 |
| 100 days | 635 | 492 | 470 | 404 | 530 | 427 | 365 |
| 114 days | 641 | 510 | 490 | 407 | 547 | 434 | 379 |
| 128 days | 650 | 525 | 505 | 410 | 556 | 439 | 383 |

**Table 5.** Water loss (by its weight percent) data for all concretes, cured at 60% RH and 25 °C.

| | H25 | M35 | M45 | F45 | SCC35 | SCC55 | SCC70 |
|---|---|---|---|---|---|---|---|
| 7 days | 1.40 | 1.19 | 0.726 | 0.48 | 0.45 | 0.25 | 0.19 |
| 14 days | 1.55 | 1.29 | 0.887 | 0.63 | 0.72 | 0.50 | 0.25 |
| 28 days | 1.67 | 1.37 | 1.25 | 0.70 | 1.19 | 0.65 | 0.32 |
| 50 days | 1.88 | 1.41 | 1.37 | 0.52 | 1.33 | 0.97 | 0.4 |
| 75 days | 1.92 | 1.52 | 1.47 | 0.1.1 | 1.44 | 1.10 | 0.5 |
| 100 days | 1.98 | 1.57 | 1.50 | 1.2 | 1.52 | 1.16 | 0.54 |
| 114 days | 2.03 | 1.60 | 1.53 | 1.21 | 1.53 | 1.17 | 0.58 |
| 128 days | 2.04 | 1.61 | 1.54 | 1.21 | 1.54 | 1.18 | 0.6 |

**Table 6.** Water loss (by its weight percent) data for all concretes, cured at 70% RH and 25 °C.

| | H25 | M35 | M45 | F45 | SCC35 | SCC55 | SCC70 |
|---|---|---|---|---|---|---|---|
| 7 days | 1.23 | 1.08 | 0.55 | 0.46 | 0.38 | 0.23 | 0.15 |
| 14 days | 1.36 | 1.28 | 0.80 | 0.58 | 0.73 | 0.37 | 0.19 |
| 28 days | 1.46 | 1.38 | 0.94 | 0.69 | 0.87 | 0.47 | 0.25 |
| 50 days | 1.59 | 1.41 | 1.13 | 0.75 | 0.95 | 0.71 | 0.30 |
| 75 days | 1.68 | 1.45 | 1.28 | 0.83 | 1.08 | 0.88 | 0.42 |
| 100 days | 1.73 | 1.47 | 1.29 | 0.92 | 1.17 | 1.06 | 0.48 |
| 114 days | 1.77 | 1.49 | 1.37 | 0.97 | 1.21 | 1.07 | 0.51 |
| 128 days | 1.78 | 1.50 | 1.38 | 0.99 | 1.23 | 1.08 | 0.53 |

by taking an average value of 4 specimens. These specimens were water cured till 28 days and here after cured in the controlled chambers where the relative humidity and temperature were controlled. The plots of the average compressive strengths with the age is as shown in the Figure 3 (water cured till 28 days, and there after cured in controlled environment of 60% and 70% RH, and 25 °C of temperature). From the figure one can observe that the F45 concrete exhibiting a prolonged increase in compressive strength due to its delayed hydration from the presence of fly ash.

### *2.4.2. Creep results*

Figure 4 shows the variation in average total creep compliance (J) for all concretes loaded at 14 days and tested at the controlled conditions of 60% RH and 25 °C. The x-axis shows the age in days $(t - t_1)$ ($t$ is the time that the creep is measured and $t_1$ is the time at application of load) in logarithmic scale and the y-axis shows the total

 https://doi.org/10.1016/j.heliyon.2018.e00698

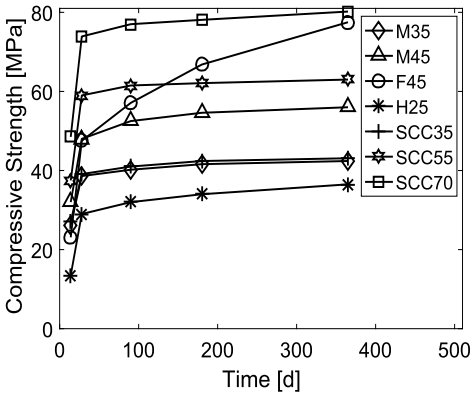


**Figure 3.** Average compressive strength of all concretes at different ages.

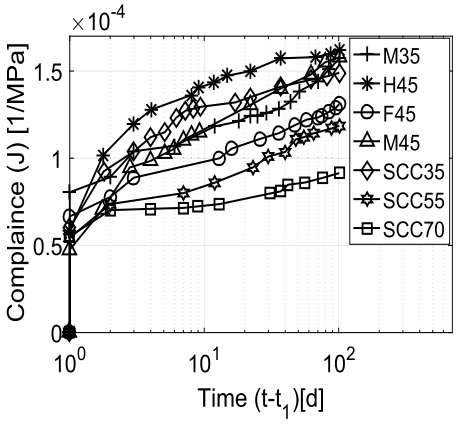


**Figure 4.** Creep strain measurements for all concretes cured at 60% RH and 25 °C temperature and loaded at 14 days.

compliance (normalized with the applied stress) in normal scale. From the Figure, it is observed that the creep strains are higher for the heavy density concrete (25 MPa) than for either normal density concrete (35 MPa or 45 MPa). This may be attributed to the hematite aggregate having a lower water absorption value [20] than the normal aggregate (granite) and this leads to a larger amounts of free water being available for drying. This free water causes more drying and results in higher drying creep strain. When comparing high volume fly ash concrete (F45) to normal vibrated concrete M45, the F45 concrete shows a lower creep strain than M45 concrete. This is firstly due to F45 concrete having lower porosity than the M45 concrete and secondly the high volume fly ash concretes shows a prolonged hydration and this increases the compressive strength beyond the 28 days of concrete age (Figure 3). The increase in compressive strength of F45 concrete shown in the Figure 3. The stiffness of F45 concrete also increases with the age due to its prolonged hydration. This is very important for practical applications of fly ash in concrete. When comparing M35 and SCC35, the SCC35 shows a higher creep than the M35 concrete. This is because of

 https://doi.org/10.1016/j.heliyon.2018.e00698

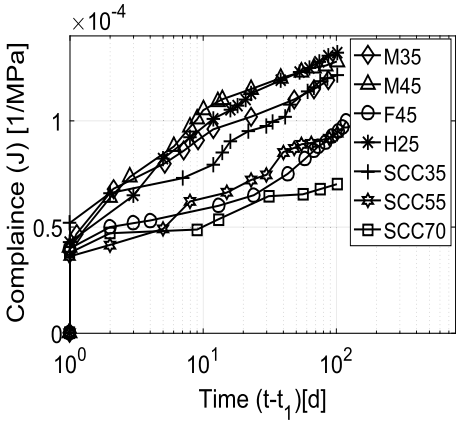


**Figure 5.** Creep strain measurements for all concretes cured at 60% RH and 25 °C temperature and loaded at 28 days.

the aggregate cement ratio (a/c) of M35 is higher than the SCC35 concrete. The more the a/c ratio in concrete exhibits lesser creep strain [21]. SCC55 concrete shows a lower creep strain than the conventional concretes (M35 and M45) and this concrete contains a 16% of fly ash replacing cement. SCC70 concrete shows lower creep strains than the other concretes including conventional (M35 and M45) and SCC concretes (SCC35 and SCC55). SCC70 concrete contains a 10% of silica fume and 16% of fly ash and this mineral admixtures making the concrete denser which results in a lower permeability. The lower permeability causes a slow drying process hence progress of drying creep is slow.

Figure 5 shows the total compliance for all the concretes that were loaded at 28 days and tested at the controlled condition of 60% RH and 25 °C. This Figure shows a lower creep strain for all the concretes loaded at 28 days, when compared to the concretes loaded at 14 days. This is because, lower age specimens have higher moisture content and there lower strength and stiffness than the higher age specimens. The more the presence of moisture content then more the drying creep. Figure 6 and 7 shows the creep strains for all concretes loaded at 14 and 28 days respectively and tested at the ambient condition of 70% RH and 25 °C. The specimens cured at lower humidities shows a higher creep strain than the specimens cured at higher humidities.

## 3. Theory

The mathematical model is inspired by the theoretical approach developed by Olivier Coussy et al. [22,23,24] that is based on a poromechanics. There are a number of differences in the model developed in the present study from that reported in the works of Coussy [22,23,24]. The differences are highlighted in the subsequent

 https://doi.org/10.1016/j.heliyon.2018.e00698

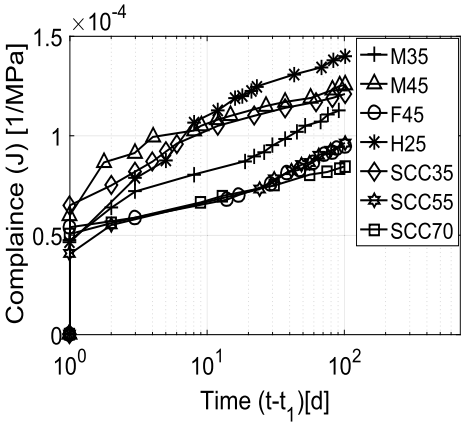


**Figure 6.** Creep strain measurements for all concretes cured at 70% RH and 25 °C temperature and loaded at 14 days.

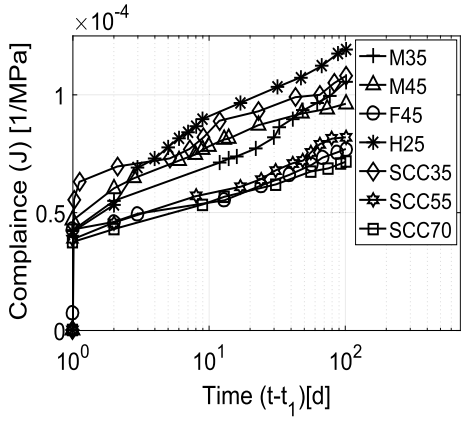


**Figure 7.** Creep strain measurements for all concretes cured at 70% RH and 25 °C temperature and loaded at 28 days.

sections. The state variables of the model are capillary pressure $p_c$, temperature T, and displacement vector u. The dependent variables are considered as a function of the degree of hydration $\alpha$.

## 3.1. General assumptions

The following assumptions have been made to develop coupled equations.

- Concrete is treated as a multiphase porous material consisting of solid skeleton, water and water vapor.
- The effect of dry air is neglected since its mass is much smaller when compared to that of water and water vapor mass.
- The voids in concrete is partially filled with water and water vapor.

 https://doi.org/10.1016/j.heliyon.2018.e00698

- The velocity of the solid skeleton is neglected, assuming that the solid skeleton velocity is much slower than the other species.

## 3.2. Governing equations

The model is developed based on a state of thermodynamic equilibrium being established locally (slow phenomena). Phase changes and chemical reactions (hydration) are taken into account in the model development. The model is partially uncoupled with the mechanical solution on capillary pressure and temperature. The model accounts for various moisture, energy and transport phenomena (Characteristic of the various phases of concrete). Evolution of material properties (porosity, permeability, strength properties) with the extent of hydration of concrete is considered in the model. Material nonlinearities due to temperature, capillary pressure, moisture content are included in this development. The model considers a representative elementary volume to describe the micro scale processes and a volume averaging theory to develop the macroscopic (space averaged) balance equations [25,26]. In the original formulation [22,23,24] the energy equation has not been considered. In the present model the energy equation is considered and coupled through Kelvin equation (specified as the equation (7) later). The present model accounts for hydration effects on concretes containing mineral admixtures which was not considered in the referred model [22,23,24]. The details of the hydration model is given in the hydration section later (section 3.4).

*Mass balance equation*:

The macroscopic balance equation of mass for the phase $\beta$ of the porous media is [22]

$$\frac{\partial\left(\rho_\beta n S_\beta\right)}{\partial t} + \bigtriangledown.\left(\rho_\beta n S_\beta \mathbf{v}_\beta\right) = 0 \tag{1}$$

Where, $\rho_\beta$ is density of the phase, $\mathbf{v}_\beta$ is the velocity of $\beta$ phase, $S_\beta$ is the saturation and $n$ is the porosity. Further,

$$\sum_\beta S_\beta = 1 \tag{2}$$

The moist concrete voids consist water (w) and water vapor (v). In the above equation $\beta$ represents these phases. Using the equation (1), the balance equation for each phase as:

Mass balance equation for water vapor:

$$\frac{\partial\left(n(1-S_w)\rho_v\right)}{\partial t} + \bigtriangledown.\left(\eta_v \rho_v \mathbf{v}_v\right) = \dot{M}_v \tag{3}$$

Mass balance equation for water:

$$\frac{\partial \left(nS_w\rho_w\right)}{\partial t} + \bigtriangledown.\left(\eta_w\rho_w\mathbf{v}_w\right) = -\dot{m}_{hydr} - \dot{M}_v \tag{4}$$

where $M_v$ is the mass source and $\dot{m}_{hydr}$ is the mass of hydration which is detailed in the hydration model section 3.4.

Combining the mass balance equation of water (equation (4)) and water vapor (equation (3)) to eliminate the vaporization source term ($M_v$), the final form of the equation becomes equation (5).

$$\frac{\partial \left(nS_w\rho_w + n(1-S_w)\rho_v\right)}{\partial t} + \bigtriangledown.\left(\eta_w\rho_w\mathbf{v}_w + \eta_v\rho_v\mathbf{v}_v\right) = -\dot{m}_{hydr} \tag{5}$$

The transport of liquid water and water vapor is assumed to be governed by Darcy's law. Then the velocity component for a phase can be written as:

$$n\mathbf{v}_\beta = -\frac{K}{\mu_\beta}k_{r\beta}\bigtriangledown p_\beta \tag{6}$$

In equation (6), K is permeability of the concrete, $k_{r\beta}$ is the relative permeability, $\mu_\beta$ and $p_\beta$ are the viscosity and pressure of each phase of the concrete.

Kelvin equation [27] to establish equilibrium between capillary water and water vapor is given in equation (7).

$$ln\left(\frac{p_v}{p_{sat}}\right) = -\frac{p_c}{\rho_w}\frac{M_w}{RT} \tag{7}$$

and

$$p_w = p_v - p_c \tag{8}$$

Where $p_v$, $p_c$, $p_{sat}$ and $p_w$ are the vapor, capillary, saturated vapor and water pressure respectively.

*Enthalpy balance equation*:

The enthalpy balance equation for a multiphase system can be defined as:

$$\left(\rho C_p\right)_{eff}\frac{\partial T}{\partial t} + \rho C_p\mathbf{v}.\bigtriangledown T - \bigtriangledown.\left(\lambda_{eff}\bigtriangledown T\right) = L_{hydr}\dot{\alpha} \tag{9}$$

with,

$$\left(\rho C_p\right)_{eff} = C_{pw}\rho_w\eta_w + C_{pv}\rho_v\eta_v + C_{ps}\rho_s\eta_s \tag{10}$$

$$\rho C_p\mathbf{v} = C_{pw}\rho_w\eta_w\left(-\frac{Kk_{rw}}{\mu_w}\bigtriangledown p_w\right) + C_{pv}\rho_v\eta_v\left(-\frac{Kk_{rg}}{\mu_g}\bigtriangledown p_v\right) \tag{11}$$

Where, $\left(\rho C_p\right)_{eff}$ is the effective volumetric heat capacity, $C_{p\beta}$ is the individual heat capacities of it's phase $\beta$. $\lambda_{eff}$ is the effective thermal capacity of the moist concrete.

 https://doi.org/10.1016/j.heliyon.2018.e00698

Using the latent heat of evaporation term in the multi phase enthalpy equation (9), the modified equation becomes

$$\left(\rho C_p\right)_{eff}\frac{\partial T}{\partial t}+\rho C_p\mathbf{v}.\bigtriangledown T-\bigtriangledown.\left(\lambda_{eff}\bigtriangledown T\right)=-h_v M_v+L_{hydr}\dot{\alpha} \tag{12}$$

Where, $h_v$ is the enthalpy of vaporization. The mass vaporization term ($M_v$) is obtained either from the equation (3) or equation (4).

*Momentum balance equation*:

Navier–Stoke's equation to describe the displacements for the multiphase material can be written as [28]:

$$\bigtriangledown\boldsymbol{\sigma}+\rho\mathbf{g}=0 \tag{13}$$

Where, $\boldsymbol{\sigma}$ is the effective stress tensor, $\rho$ is the density of the multi phase material and $\mathbf{g}$ is the acceleration due to gravity. The mass density $\rho$ of multi phase system can be described as [29]:

$$\rho=(1-n)\rho_s+nS_w\rho_w+n(1-S_w)\rho_v \tag{14}$$

The state equations after introducing the constitutive relationships, in final form are as follows:

*Mass balance equation for water and water vapor phase:*

$$\begin{aligned}&\frac{\left(\rho_w S_w\right)}{\partial t}+\frac{\partial\left(n\left(1-S_w\right)\rho_v\right)}{\partial t}-\bigtriangledown.\left(\rho_w\frac{Kk_{rw}}{\mu_w}\bigtriangledown\left(p_v-p_c\right)\right)\\&-\bigtriangledown.\left(\rho_v\frac{Kk_{rg}}{\mu_g}\bigtriangledown p_v\right)=\dot{m}_{hydr}\end{aligned} \tag{15}$$

*Enthalpy balance equation*

The final farm of the enthalpy balance equation for the multi phase system is defined in the equation (16).

$$\begin{aligned}&\left(\rho C_p\right)_{eff}\frac{\partial T}{\partial t}+C_{pw}\rho_w\eta_w\left(-\frac{Kk_{rw}}{\mu_w}\bigtriangledown p_w\right).\bigtriangledown T\\&+C_{pv}\rho_v\eta_v\left(-\frac{Kk_{rg}}{\mu_g}\bigtriangledown p_v\right).\bigtriangledown T\\&+h_v\left(\frac{\rho_w S_w}{\partial t}\right)-h_v\left(\bigtriangledown.\left(\rho_w\frac{Kk_{rw}}{\mu_w}\bigtriangledown\left(p_g-p_c\right)\right)\right)\\&-h_v\left(\dot{m}_{hydr}\right)-\bigtriangledown.\left(\lambda_{eff}\bigtriangledown T\right)=L_{hydr}\dot{\alpha}\end{aligned} \tag{16}$$

*Linear momentum balance equation*

$$\bigtriangledown\boldsymbol{\sigma}+\rho\mathbf{g}=0 \tag{17}$$

### 3.2.1. Initial and boundary conditions

The initial conditions of the primary variables are specified at time $t = 0$ on both domain $\Omega$ and boundary $\Gamma$. The boundary conditions of the problem can be described as Dirichlet or Cauchy's type boundary conditions.

*The Dirichlet type boundary conditions are:*

$$\begin{aligned} &p_c(t) = \bar{p}_c(t) \quad \text{on} \quad \Gamma \\ &T(t) = \bar{T}(t) \quad \text{on} \quad \Gamma \\ &\mathbf{u}(t) = \bar{\mathbf{u}}(t) \quad \text{on} \quad \Gamma \end{aligned} \tag{18}$$

*The Cauchy type boundary conditions are defined as:*

$$\begin{aligned} &(\rho_w \eta_w \mathbf{v}_w + \rho_v \eta_v \mathbf{v}_v + \mathbf{J}_v).\mathbf{n} = q_w + q_v + \beta_s(\rho_v - \rho_{v\infty}) \quad \text{on} \quad \Gamma \\ &(\rho_w \mathbf{v}_w h_v - \lambda_{eff} \bigtriangledown T).\mathbf{n} = q_T + \alpha_c(T - T_\infty) + e\sigma_0(T^4 - T_\infty^4) \quad \text{on} \quad \Gamma \\ &\boldsymbol{\sigma}.\boldsymbol{n} = \bar{\mathbf{t}} \quad \text{on} \quad \Gamma \end{aligned} \tag{19}$$

Where $\mathbf{n}$ refers the unit normal vector, $\bar{\mathbf{t}}$ is the traction applied on the boundary, $\rho_{v\infty}$ is the mass concentration of vapor in the surrounding environment and $T_\infty$ is the environmental temperature. $e$ is the emissivity, $\sigma_0$ is the Stephen–Boltzmann constant, $\alpha_c$ is the heat exchange coefficient, $\beta_c$ is the mass exchange coefficients of vapor. $q_w$, $q_v$ and $q_T$ are the flux of water, vapor and temperature respectively.

Galarkin weighted residual finite element procedure is used to convert the above set of partial differential equations in to weak form equations. The final form the equations in the form of coefficient matrices is represented through equation (20).

$$\mathbf{C}\dot{\mathbf{x}} + \mathbf{K}\mathbf{x} = \mathbf{f} \tag{20}$$

where,

$$\mathbf{C} = \begin{pmatrix} \mathbf{C_{vv}} & 0 & 0 \\ \mathbf{C_{tv}} & \mathbf{C_{tt}} & 0 \\ 0 & 0 & 0 \end{pmatrix} \mathbf{K} = \begin{pmatrix} \mathbf{K_{vv}} & \mathbf{K_{vt}} & 0 \\ \mathbf{K_{vp}} & \mathbf{K_{vt}} & 0 \\ 0 & 0 & \mathbf{K_{uu}} \end{pmatrix} \mathbf{f} = \begin{pmatrix} \mathbf{f_v} \\ \mathbf{f_t} \\ \mathbf{f_u} \end{pmatrix}$$

Coefficients of the matrices $\mathbf{C}$, $\mathbf{K}$ and $\mathbf{f}$ are as follows:

$$\boldsymbol{C_{vv}} = \int_\Omega \boldsymbol{N_v^T} \left[ \frac{\left(\rho_w S_w n\right)}{\partial t} \boldsymbol{N_v} + \frac{\partial \left(n\left(1 - S_w\right)\rho_v\right)}{\partial t} \boldsymbol{N_v} \right] d\Omega \tag{21}$$

$$\boldsymbol{C_{tt}} = \boldsymbol{N_t^T} \left[ \left(\rho C_p\right)_{eff} \boldsymbol{N_t} + h_v \left( \frac{\rho_w n \partial S_w}{\partial T} \right) \boldsymbol{N_t} \right] d\Omega \tag{22}$$

$$\boldsymbol{C_{tv}} = \boldsymbol{N_t^T} \left[ h_v \frac{\left(\rho_w n S_w\right)}{\partial p_v} \boldsymbol{N_v} \right] d\Omega \tag{23}$$

$$\boldsymbol{K_{vv}} = \int_{\Omega} \left(\nabla \boldsymbol{N_v}\right)^T \left[\left(\rho_w \frac{\mathbf{K} k_{rw}}{\mu_w}\left(-1 + \frac{\partial p_c}{\partial p_v}\right) + \rho_v \frac{\mathbf{K} k_{rg}}{\mu_g}\right) \nabla \boldsymbol{N_v}\right] d\Omega \tag{24}$$

$$\boldsymbol{K_{vt}} = \int_{\Omega} \left(\nabla \boldsymbol{N_v}\right)^T \left[\left(\rho_w \frac{\mathbf{K} k_{rw}}{\mu_w}\left(-\frac{\partial p_c}{\partial T}\right)\right) \nabla \boldsymbol{N_t}\right] d\Omega \tag{25}$$

$$\boldsymbol{K_{tt}} = \int_{\Omega} \left(\nabla \boldsymbol{N_t}\right)^T \left[\lambda_{\mathbf{eff}} \nabla \boldsymbol{N_t}\right] d\Omega \tag{26}$$

$$\begin{aligned}\boldsymbol{K_{tv}} = & \int_{\Omega} \left(\nabla \boldsymbol{N_t}\right)^T \left[\left(\rho_w \frac{\mathbf{k} k_{rw}}{\mu_w}\left(-1 + \frac{\partial p_c}{\partial p_v}\right) h_v\right) \nabla \boldsymbol{N_v}\right] d\Omega \\ & + \int_{\Omega} \left(\boldsymbol{N_t}\right)^T \left[\left[\left(C_{pw} \rho_w \left(\frac{K k_r w}{\mu_w}\left(-1 + \frac{\partial p_c}{\partial p_v}\right)\right)\right) \nabla \boldsymbol{N_v}\right] . \nabla T\right] d\Omega \\ & + \int_{\Omega} \left(\boldsymbol{N_t}\right)^T \left[\left[\left(C_{pv} \rho_v \left(\frac{K k_r g}{\mu_g} \nabla\right)\right) \nabla \boldsymbol{N_v}\right] . \nabla T\right] d\Omega\end{aligned} \tag{27}$$

$$\boldsymbol{K_{uu}} = -\int_{\Omega} \boldsymbol{B^T C B}\, d\Omega \tag{28}$$

$$\boldsymbol{f_v} = \int_{\Omega} \left(\boldsymbol{N_v}\right)^T \left[-m_{hydr}\right] d\Omega + \int_{\Gamma} \boldsymbol{N_v^T} \left[q_w + q_v + \beta_s(\rho_v - \rho_{v\infty})\right] d\Gamma \tag{29}$$

$$\boldsymbol{f_t} = \int_{\Omega} \left(\boldsymbol{N_t}\right)^T \left[h_{de}(-m_{hydr})\right] d\Omega - \int_{\Gamma} \boldsymbol{N_t^T} \left[q_T + \alpha_c(T - T_\infty) + e\sigma_0(T^4 - T_\infty^4)\right] d\Gamma \tag{30}$$

$$\boldsymbol{f_u} = \int_{\Omega} \left(\boldsymbol{N_u}\right)^T \rho \mathbf{g} d\Omega + \int_{\Gamma} \boldsymbol{N_u}^T . \bar{\mathbf{t}}\, d\Gamma \tag{31}$$

The above discretized equation (20) have been implemented on COMSOL® interfaced with MATLAB® to obtain the solutions.

## 3.3. Material transport properties of concrete

### *3.3.1. Sorption/desorption isotherms and water content*

Sorption/desorption isotherm gives the relation between relative humidity and water content of the porous material. According to the literature ([30,31,32]) there are several formulations available to describe the sorption/desorption of the concrete. In the present model sorption /desorption isotherms proposed by Baroghel-Bounya et al. [24] is adopted. This formulation describes the sorption/desorption isotherms for normal and high performance concrete. This relationship described in the equation (32).

$$p_c\left(S_w\right) = a\left(S_w^{-b} - 1\right)^{1-1/b} \tag{32}$$

Where, 'a' and 'b' are the material constants, it is estimated from the experiments.

### 3.3.2. Permeability

The permeability of concrete is defined as a function of hydration [2]. The permeability of a concrete can be defined as:

$$k = k_{\infty} 10^{A_{kn}\alpha} \tag{33}$$

Where, $k_{\infty}$ is the permeability of concrete when the degree of hydration is unity and $A_{kn}$ is the material parameter, generally its value taken as in the range of 6 to 10.

### 3.3.3. Relative permeability

Relative permeabilities of water and gas can be defined through the equations (34) and (35) [24].

$$k_{rw} = \sqrt{S_w}\left(1 - \left(1 - (S_w)^b\right)^{1/b}\right)^2 \tag{34}$$

$$k_{rw} = \sqrt{1 - S_w}\left(1 - (S_w)^b\right)^{2/b} \tag{35}$$

Where, $k_{rw}$ and $k_{rg}$ are the relative permeability of water and gas respectively. 'a' and 'b' are the constants, which are depended on the type of concrete.

### 3.3.4. Saturated water vapor pressure

The saturated water vapor expression as a function of temperature is defined as [33]:

$$p_{sat} = p_{atm} exp\left(\frac{\triangle H}{T}\frac{T - 373.15}{373.15T}\right) \tag{36}$$

with $\triangle H = 39583.85$ J/mol.

### 3.3.5. Density of water

The expression to estimate the density of water is given by the Furbish [34] is as shown in the equation (37).

$$\begin{aligned}\rho_w = &\left(b_0 + b_1T + b_2T^2 + b_3T^3 + b_4T^4 + b_5T^5\right)\\ &+ \left(p_1 - p_{ref}\right)\left(a_0 + a_1T + a_2T^2 + a_3T^3 + a_4T^4 + a_5T^5\right)\end{aligned} \tag{37}$$

Where, $\rho_w$ is the density of water, $p_1 = 1 \times 10^7$ Pa, $p_{ref} = 2 \times 10^7$ Pa, $a_0 = 4.89 \times 10^7$, $a_1 = -1.65 \times 10^{-9}$, $a_2 = 1.86 \times 10^{-12}$, $a_3 = 2.43 \times 10^{-13}$, $a_4 = -1.60 \times 10^{-15}$, $a_5 = 3.37 \times 10^{-18}$, $b_0 = 1.02 \times 10^{-3}$, $b_1 = -7.74 \times 10^{-1}$, $b_2 = 8.77 \times 10^{-3}$, $b_3 = -9.21 \times 10^{-5}$, $b_4 = 3.35 \times 10^{-7}$ and $b_5 = -4.4 \times 10^{-10}$.

 https://doi.org/10.1016/j.heliyon.2018.e00698

### 3.3.6. Porosity

The porosity of the concrete during the hydration can be defined as [2]:

$$n = n_{\infty} A_n (1 - \alpha) \tag{38}$$

Where, $n$ is the porosity, $n_{\infty}$ is the porosity of concrete when the degree of hydration is unity and $A_n$ is the empirical constant, it is determined from the experimental data. In the present study, $n_{\infty}$ is estimated based on ASTM C642-13 standard [35].

### 3.3.7. Thermal conductivity

The thermal conductivity of the moist concrete can be defined as [36]:

$$\lambda_{eff} = \lambda_d \left( 1 + \frac{4 n \rho_w S_w}{(1 - n) \rho_s} \right) \tag{39}$$

Where, $\lambda_d$ is the thermal conductivity of the dry material and it is approximated through the experimental data.

### 3.3.8. Enthalpy of vaporization

The enthalpy of vaporization of water is calculated by using Watson formula [37]. This expression is defined as:

$$h_v = 2.672 \times 10^5 \left( T - T_{cr} \right)^{0.38} \tag{40}$$

Where, $h_v$ is the enthalpy of vaporization and $T_{cr}$ is the critical point temperature of water and its value is 647.30 K.

## 3.4. Hydration model

The properties of concrete such as compressive strength ($f_c$) Poison's ratio ($\nu$), elastic modulus ($E$) etc. depends on the degree of hydration of cementitious material. It is very important to model hydration accurately to describe the material properties.

### 3.4.1. Hydration model for Portland cement

The Arrhenius equation is used to model the ordinary Portland cement (OPC). The effects of fineness of cement, chemical composition, water to cement ratio and curing temperature is considered in the model [3,38,39]. The effects of environmental conditions on the cement hydration is considered by incorporating the appropriate

 https://doi.org/10.1016/j.heliyon.2018.e00698

boundary conditions (B.C.'s). The details of the hydration model for OPC is as follows:

Arrhenius equation

$$\dot{\alpha} = A_\alpha \beta_\alpha exp\left(-\frac{E_a}{RT}\right) \tag{41}$$

where $\alpha$ is the hydration degree, $E_a$ is the activation energy which depends on the chemical composition of the cement, $R$ is the universal gas constant. $\beta_\alpha$ is the permeability of the hydration products around the unhydrated cement. $A_\alpha$ represents the chemical affinity which is defined as in equation (42).

$$A_\alpha(\alpha, Blaine, w/c) = k_1\left(\frac{A_0}{k_1\alpha_u} + \alpha\right)(\alpha_u - \alpha) \tag{42}$$

In equation (42), $A_0$ is a function of Blaine's fineness and chemical composition of the cement, which is defined in equation (43), $k_1$ is the material constant which is also a function of chemical composition defined in equation (44).

$$A_0 = \frac{A_0^c \times Blaine}{350} \tag{43}$$

$$k_1 = 0.56 \times \left(p_{C_3S}\right)^{-0.206} \times \left(p_{C_2S}\right)^{-0.128} \times \left(p_{C_3A}\right)^{0.161} \tag{44}$$

where $A_0^c$ is the normalized affinity of cement and is a function of chemical composition of cement, which can be defined as

$$A_0^c = -0.0767 p_{C_4AF} + 0.0184 \tag{45}$$

where $p_{C_4AF}$ is a Bogue mass fraction of $C_4AF$.

In equation (41) $\beta_\alpha$ is defined as

$$\beta_\alpha = exp(-\phi\alpha) \tag{46}$$

where $\phi$ is the parameter related to a function of hydration degree and curing temperature, which can be defined as

$$\phi = \phi_0 f_1 f_2 \tag{47}$$

In equation (47), $\phi_0$ is a material constant which is a function of chemical composition of the cement given in equation (48). $f_1$ and $f_2$ are the parameters that depends on Blaine's fineness, hydration degree and temperature, which is defined in equation (49) and (50) respectively.

$$\phi_0 = 10.945 p_{C_3S} + 11.25 p_{C_2S} - 4.10 p_{C_3A} - 0.892 \tag{48}$$

$$f_1 = 1 + (1-\alpha)^2 ln\left(\frac{350}{Blaine}\right) \tag{49}$$

$$f_2 = \left(\frac{C_{293.15}}{C(T)}\right)^{10\alpha^4} \tag{50}$$

 https://doi.org/10.1016/j.heliyon.2018.e00698

where $C$ is the ratio of volume of hydrated products and reacted cement which can be defined as

$$C(T) = C_{293.15} exp\left[-28 \times 10^{-6}\,(T - 293.15)^2\right] \tag{51}$$

Where $C_{293.15}$ is the volume of hydration products to reacted cement at the temperature of 293.15 K, generally this value is taken as 2.2, according to Powers and Brownyard [40]. The apparent activation energy $E_a$ proposed by Schindler [41] is given in the equation (52).

$$E_a = 22100 \times \left(p_{C_3A}\right)^{0.30} \times \left(p_{C_4AF}\right)^{0.25} \times (Blaine)^{0.35} \tag{52}$$

Where $p_{C_3A}$ is the weight ratio of $C_3A$ with respect to total cement content, $p_{C_4AF}$ is the weight ratio of $C_4AF$ with respect to total cement content and Blaine value is the specific surface area of cement ($m^2$/kg).

In equation (42), $\alpha_u$ is the ultimate degree of hydration given by Lin and Meyer [42] is as defined in equation (53). This equation accounts for the effects of Blaine's fineness of the cement and curing temperature while calculating the ultimate degree of hydration.

$$\alpha_u = \alpha_{u,293} exp\left[-0.000003(T - 293)^2 . SGN(T - 293)\right] \tag{53}$$

and

$$SGN(T - 293) = \begin{cases} 1 & \text{if } T \geq 293 \text{ K} \\ -1 & \text{if } < 293 \text{ K} \end{cases}$$

$\alpha_{u,293}$ accounts for the fineness of the cement and this can be defined as:

$$\alpha_{u,293} = \frac{\beta_1(Blaine)w/c}{\beta_2(Blaine) + w/c} \tag{54}$$

with,

$$\beta_1(Blaine) = \frac{10}{9.33(\frac{Blaine}{100})^{-2.82} + 0.38} \tag{55}$$

and

$$\beta_1(Blaine) = \frac{Blaine - 220}{147.78 + 1.656(Blaine - 220)} \tag{56}$$

$\beta_1(Blaine)$ and $\beta_2(Blaine)$ are valid only for Blaine's fineness is above 270 $m^2$/kg. If the Blaine fineness is below 270 $m^2$/kg, $\beta_1$ and $\beta_2$ is assumed to be a constant, that can be defined as:

$$\beta_1(Blaine < 270) = \beta_1(Blaine = 270) \tag{57}$$

 https://doi.org/10.1016/j.heliyon.2018.e00698

and

$$\beta_2(Blaine < 270) = \beta_2(Blaine = 270) \tag{58}$$

### 3.4.2. Hydration model for fly ash as a mineral admixture

Based on the composition of the fly ash, Schindler [41] proposed correction factor in the activation energy ($E_a$) in the hydration equation (41). This correction in activation energy has been used in the present model along with cement hydration model.

$$E_{af} = 22100 \times f_E \times \left(p_{C_3A}\right)^{0.30} \times \left(p_{C_4AF}\right)^{0.25} \times (Blaine)^{0.35} \tag{59}$$

where $E_{af}$ is the activation energy of cementitious material containing fly ash, $f_E$ is the correction factor which is given in equation (60)

$$f_E = 1 - 1.05 \times p_{FA}\left(1 - \frac{p_{FACaO}}{0.40}\right) \tag{60}$$

where $p_{FA}$ is the weight fraction of fly ash with respect to total cementitious material and $p_{FACaO}$ is the weight fraction of the $CaO$ content of the fly ash. Total hydration of the blended cement containing fly ash can be written using equation (41) as:

$$\dot{\alpha} = A_\alpha \beta_\alpha exp\left(-\frac{E_{af}}{RT}\right) \tag{61}$$

### 3.4.3. Ultimate degree of hydration for fly ash containing cements

The ultimate degree of hydration ($\alpha_{uf}$) for blended cement containing fly ash is given by the Schindler [41], can be written as:

$$\dot{\alpha_{uf}} = \text{ultimate degree of cement} + 0.5(p_{FA}) \leq 0 \tag{62}$$

where $p_{FA}$ is the volume fraction of fly ash in terms of total ostentatious content.

## 3.5. Hydration model for silica fume as a mineral admixture

The silica fume (SF) reaction modeled same as cement hydration model. The Arrhenius type equation proposed by Lizio [43] is stated in the equation (63).

$$\dot{\alpha_s} = A_{\alpha_s} \beta_{\alpha_s} exp\left(-\frac{E_{as}}{RT}\right) \tag{63}$$

where $\alpha_s$ is the hydration of silica fume, $A_{\alpha_s}$ is the SF affinity which is given in the equation (64), $E_{as}$ is the activation energy of SF, $\beta_{\alpha_s}$ is the material constant, which is given in the equation (65).

 https://doi.org/10.1016/j.heliyon.2018.e00698

$$A_{\alpha_s} = k_{s1}\left(\frac{A_{s0}}{\alpha_{us}} + \alpha_s\right)\left(\alpha_{us} - \alpha_s\right) \tag{64}$$

$$\beta_{\alpha_s} = exp\left(-\eta_s \frac{\alpha_s}{\alpha_{us}}\right) \tag{65}$$

where $k_{s1}$, $A_{s0}$ and $\eta_s$ are the experimentally computed material constants are given by Yajun [44]. $\alpha_{us}$ is the ultimate degree of SF reaction, this is defined in equation (66) given by Yajun [44] and Luzio [43].

$$\beta_{\alpha_u s} = SF^{eff}\, min\left[1, \frac{(s/c)_{req}}{s/c}\right] \tag{66}$$

and

$$SF^{eff} = min\,(0.16, 0.4w/c) \tag{67}$$

According to Yajun [44], all the calcium hydroxide (CH) produced during the cement hydration can consumed by the pozzolanic reaction when sufficient amount of SF available in the mixture. Silica fume to cement ratio (s/c) equal to 0.16 is required to consume all the CH during the pozzolanic reaction when water to cement ratio (w/c) of about 0.5. If the w/c ratio is less than the required SF ($(s/c)_{req}$) to consume all the CH will be reduced proportionally. The Proportionality coefficient 0.4 were used in the equation (67).

## 3.6. Heat of hydration

### *3.6.1. Heat of hydration of cement:*

Based on the cement composition Bogue [45] proposed an expression to estimate the total heat of hydration of cement at complete hydration. This expression is represented as:

$$L_{hydr} = 500\times p_{C_3S} + 866\times p_{C_3A} + 624\times p_{SO_3} + 1186\times p_{FreeCaO} + 850\times p_{MgO} \tag{68}$$

Where, $L_{hydr}$ is the latent heat of hydration (J/g) when all the cement completely get hydrated, $p_i$ is the weight fraction of $i$th compound with respect to total cement content.

### *3.6.2. Heat of hydration of fly ash and silica fume:*

According to Schindler [41], the heat of hydration per gram of fly ash ($L_{Fa}$) reaction is given based on the percentage of $CaO$ present in the fly ash.

$$L_{FA} = p_{CaO} * 1800/100 \tag{69}$$

For silica fume the latent heat of hydration given by Waller [46] as 870 J/g.

 https://doi.org/10.1016/j.heliyon.2018.e00698

### 3.6.3. Heat of hydration for blended cement containing fly ash and silica fume

Using equations (68) and (69), and by considering the enthalpy of silica fume, the total enthalpy of blended cement can be written as:

$$L_{hydr} = p_c \times L_{cem} + p_{FA} \times L_{FA} + 870 \times p_{SF} \tag{70}$$

Where, $p_c$, $p_{FA}$ and $p_{SF}$ is the weight fraction of cement, fly ash and silica fume respectively for blended cement. Equation (70) is used to calculate the total heat of hydration in the enthalpy balance equation (9).

## 3.7. Mass of hydrated water

From the experimental studies, it is found that the 0.23 g of water is required to hydrate 1 g of cement completely [40,47,48,49]. According to Maekawa [50], the mass of hydrated water required to hydrate 1 g of fly ash is 0.1 g. This can be described as:

$$m_{hydr} = 0.23 \times c + 0.1 \times FA \tag{71}$$

Where, $m_{hydr}$ is the mass of hydrated water, $c$ and $FA$ are cement and fly ash content of the mix respectively. This relationship is used to calculate the hydrated water quantity in the mass balance equation (15) as a source term.

## 3.8. Modeling of creep

For modeling creep, a micro-prestress solidification (MPS) theory proposed by Bazant and Prasannan [51,52] is used. According to MPS theory, the total strain rate can be written as

$$\dot{\epsilon} = \dot{\epsilon_e} + \dot{\epsilon_c} + \dot{\epsilon_f} + \dot{\epsilon_d} + \dot{\epsilon_{sh}} + \dot{\epsilon_T} \tag{72}$$

where $\dot{\epsilon}$ is the total strain rate, $\dot{\epsilon_e}$ is the instantaneous elastic strain rate, $\dot{\epsilon_c}$ is the viscoelastic strain, $\dot{\epsilon_f}$ is the viscous flow strain rate, $\dot{\epsilon_d}$ is the inelastic strain rate due to damage and cracking, $\dot{\epsilon_{sh}}$ is the Shrinkage strain rate and $\dot{\epsilon_T}$ is the rate of thermal strain. The rheological representation of these strains with constant stress as shown in the Figure 8.

In Figure 8 the spring element represents the elastic strain ($\epsilon_e$), the series of kelvin elements represents the basic creep ($\epsilon_v$), the slider represents the thermal ($\epsilon_T$) and shrinkage strain ($\epsilon_{sh}$) and the dash pot element represents the viscous flow strain ($\epsilon_f$).

 https://doi.org/10.1016/j.heliyon.2018.e00698

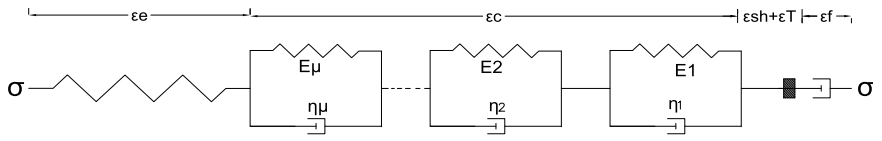


**Figure 8.** Schematic rheological representation of total strain.

### 3.8.1. Instantaneous elastic strain rate

The instantaneous elastic strain rate is the strain that occurs immediately after the stress rate applied, which can be written as

$$\dot{\epsilon_e} = q_1 G \dot{\sigma} \tag{73}$$

Where, $q_1$ is the material parameter, which depends on the elastic modulus of the concrete. Present model $q_1$ treated as a function of hydration degree. $G$ is a constitutive matrix which is defined as:

$$G = \begin{pmatrix} 1 & -\nu & -\nu & 0 & 0 & 0 \\ -\nu & 1 & -\nu & 0 & 0 & 0 \\ -\nu & -\nu & 1 & 0 & 0 & 0 \\ 0 & 0 & 0 & 2(1+\nu) & 0 & 0 \\ 0 & 0 & 0 & 0 & 2(1+\nu) & 0 \\ 0 & 0 & 0 & 0 & 0 & 2(1+\nu) \end{pmatrix}$$

Poisson's ratio ($\nu$) of 0.19 used in this model for concrete as a material.

### 3.8.2. Basic creep (visco elastic strain rate, $\dot{\epsilon_v}$)

The basic creep is modeled using a series of kelvin units schematically shown in the Figure 8. This can be written as

$$\dot{\epsilon_v} = \frac{1}{\vartheta}\dot{\gamma} \tag{74}$$

and

$$\gamma = \sum_{\mu=1}^{N} \gamma_\mu \tag{75}$$

$$\phi\left(t, t'\right) = \sum_{\mu}^{N} A_\mu \left[1 - exp\left(-\left(t - t'\right)/\tau_\mu\right)\right] \tag{76}$$

with

$$A_\mu = \frac{1}{E_\mu} \tag{77}$$

where, $\gamma_\mu$ is the visco-elastic micro strain of $\mu$th Kelvin unit and $E_\mu$ is the elastic modulus of $\mu$th Kelvin unit which is defined as

 https://doi.org/10.1016/j.heliyon.2018.e00698

$$A_{\mu} = \frac{1}{E_{\mu}} = L\left(\tau_{\mu}\right) ln\left(10\right) \triangle \left(log\tau_{\mu}\right) \tag{78}$$

$L\left(\tau_{\mu}\right)$ can be calculated using continuous retardation spectrum for concrete given by Bazant and Yunping [53] can be written as

$$L\left(\tau_{\mu}\right) = q_2 N\left(N-1\right) \frac{\left(3\tau_{\mu}\right)^N}{1+\left(3\tau_{\mu}\right)^N} \tag{79}$$

where $N$ is the number of kelvin units ($N$ = 1,2,3...N), $q_2$ is the material constant and which is a function of cement content and compressive strength of concrete. $\tau_{\mu}$ is the retardation time which can be calculated using the equation (80)

$$\tau_{\mu+1} = 10\tau_{\mu} \tag{80}$$

### 3.8.3. Aging creep (viscous flow strain $\epsilon_f$)

The aging creep is modeled using a dash-pot element. The dash-pot variable i.e., viscosity ($\eta$) is calculated from the differential equation given in equation (81).

$$\dot{\eta} + \frac{1}{\mu_S T_0}\left|T\frac{\dot{h}}{h} + ln(h)\dot{T}\right|\left(\mu_S \eta\right)^{p/(p-1)} = \frac{\Psi_S}{q_4} \tag{81}$$

where $\eta$ is the viscosity, $h$ is the humidity, $q_4$ is the material constant and which is a function of aggregate cement ratio (a/c). $p$ is a constant, this value generally taken as 2, $\mu_s$ is given in the equation (82)

$$\mu_s = c_0 T_0^{p-1} k_1^{p-1} q_4 \left(p-1\right)^p \tag{82}$$

where $k_1$, $c_0$ are constants, the $\psi$ is defined in the equation (83)

$$\psi(t) = \beta_{sT}\beta_{sh} \tag{83}$$

with

$$\beta_{sT} = exp\left[\frac{Q_s}{R}\left(\frac{1}{T_0} - \frac{1}{T}\right)\right] \tag{84}$$

and

$$\beta_{sh} = \alpha_s + \left(1-\alpha_s\right)h^2 \tag{85}$$

where $Q_s$ is the activation energy and $\alpha_s$ is the material parameter.

 https://doi.org/10.1016/j.heliyon.2018.e00698

### 3.8.4. Shrinkage ($\epsilon_{sh}$) and thermal ($\epsilon_T$) strains

The thermal strain can be modeled using the equation

$$\dot{\epsilon_T} = \alpha_T \dot{T} \tag{86}$$

where $\alpha_T$ is the thermal expansion coefficient. Shrinkage strain can be written as:

$$\dot{\epsilon_{sh}} = k_{sh} \dot{h} \tag{87}$$

where $k_{sh}$ is the shrinkage coefficient.

## 3.9. Willam–Warnke yield criterion

The above model is combined with Willam–Warnke [54] yield criterion to capture failure surface. According to Willam–Warnke [54], the three parameter failure criterion defined as:

$$F_w = \sqrt{\frac{3}{5}} \frac{\tau_o}{f_c} + r(\theta) \left[ \left( \frac{1}{f_t} - \frac{1}{f_b} \right) \sigma_o - 1 \right] = 0 \tag{88}$$

where $f_c$ is the uniaxial compressive strength, $f_t$ is the uniaxial tensile strength and $f_b$ is the biaxial compressive strength of the concrete. The octahedral shear ($\tau_o$) and normal ($\sigma_o$) stresses of the concrete expressed as:

$$\sigma_o = \frac{I_1}{3} \text{ and } \tau_o = \sqrt{\frac{2J_2}{3}} \tag{89}$$

where $I_1$ is the first principle stress invariant and $J_2$ is the second deviatoric stress invariant. In the equation (88), $\theta$ is the Lode angle and $r(\theta)$ is the segment of an ellipse on the octahedral plane and it can be defined as:

$$r(\theta) = \frac{\left( 2r_c(r_c^2 - r_t^2)cos\theta + r_c \left( 2r_t - r_c \right) \sqrt{4 \left( r_c^2 - r_t^2 \right) cos^2\theta + 5r_t^2 - 4r_c r_t} \right)}{4 \left( r_c^2 - r_t^2 \right) cos^2\theta + \left( r_c - 2r_t \right)^2} \tag{90}$$

where $r_c$ and $r_t$ are the compressive and tensile meridian and can be written as:

$$r_t = \sqrt{\frac{6}{5}} \frac{f_b f_t}{2f_b f_c + f_t f_c} \tag{91}$$

and,

$$r_c = \sqrt{\frac{6}{5}} \frac{f_b f_t}{3f_b f_t + f_b f_c - f_t f_c} \tag{92}$$

**Table 7.** Properties of different types of concretes that used in the numerical simulations.

| Parameter | Unit | M35 | M45 | F45 | SCC35 | SCC55 | SCC70 | H25 |
|---|---|---|---|---|---|---|---|---|
| n | [%] | 18.5 | 15.2 | 15 | 16 | 13.2 | 11.5 | 16.5 |
| K | [$m^2$] | $1.6 \times 10^{-17}$ | $1.6 \times 10^{-17}$ | $1 \times 10^{-17}$ | $1.8 \times 10^{-17}$ | $1 \times 10^{-17}$ | $0.9 \times 10^{-18}$ | $1.8 \times 10^{-17}$ |
| $E_a$ | [J/mol] | 46029 | 46029 | 31530 | 46029 | 38780 | 39227 | 46029 |
| $L_{hydr}$ | [J/g] | 472.9 | 472.9 | 350 | 472.9 | 426.28 | 489.69 | 472.9 |
| $\phi_0$ | 6.7 | 6.7 | 6.7 | 6.7 | 6.7 | 6.7 | 6.7 | 6.7 |
| $A_0^c$ | [-] | 0.0122 | 0.0122 | 0.0122 | 0.0122 | 0.0122 | 0.0122 | 0.0122 |
| $k_1$ | [h] | 0.53 | 0.53 | 0.53 | 0.53 | 0.53 | 0.53 | 0.53 |
| $a$ | [-] | 18.637 | 18.6237 | 46.9364 | 18.6237 | 46.9364 | 46.9364 | 18.6237 |
| $b$ | [-] | 2.2748 | 2.2748 | 2.0601 | 2.2748 | 2.0601 | 2.0601 | 2.2748 |
| $\rho$ | [kg/$m^3$] | 2320 | 2232 | 2351 | 2113 | 2094 | 2166 | 3602 |
| $\lambda_{eff}$ | [W/(m K)] | 1.6 | 1.6 | 1.8 | 1.6 | 1.8 | 1.8 | 2.1 |
| $(C_p)_{eff}$ | [J/(kg K)] | 1020 | 1020 | 1020 | 1020 | 1020 | 1020 | 1500 |
| *Blaine* | [$m^2$/kg] | 372 | 372 | 372 | 372 | 372 | 372 | 372 |
| $\alpha_u$ | [-] | 0.91 | 0.89 | 0.91 | 0.91 | 0.88 | 0.89 | 0.91 |
| $\mu_s$ | [1/(Pa*s)] | $1.49 \times 10^{-9}$ | $1.62 \times 10^{-9}$ | $1.34 \times 10^{-9}$ | $1.60 \times 10^{-9}$ | $1.55 \times 10^{-9}$ | $1.79 \times 10^{-9}$ | $1.25 \times 10^{-9}$ |
| $k_{sh}$ | [-] | $6.14 \times 10^{-4}$ | $6.51 \times 10^{-4}$ | $1.20 \times 10^{-4}$ | $5.91 \times 10^{-4}$ | $2.13 \times 10^{-4}$ | $0.76 \times 10^{-4}$ | $9.27 \times 10^{-4}$ |
| $(f_c)_{28}$ | [MPa] | 38.6 | 55.1 | 51.2 | 39.1 | 59 | 73.9 | 32.1 |
| $(E)_{28}$ | [GPa] | 30 | 37 | 32 | 30 | 31 | 33 | 30 |

Note: (i) the material properties $n$, is estimated through the porosity tests conducted in this study. $K$ is estimated based on the drying tests conducted in present study. $\rho$ is estimated based on the material proportion that specified in the concrete mixes, $(f)_{c,28}$ and $(E)_{28}$ were estimated from the strength tests from the present study. (ii) $Ea$ is calculated from the paper [41], $L_{hydr}$ is calculated from the papers [45,46,55]. The parameters, $\phi_0$, $k_1$ and $A_0^c$ are estimated from the paper Lin and Meyer [38]. $\lambda_{eff}$ and $(C_p)_{eff}$ for all the concretes except H25 mix taken from the paper Gawin et al. [2], $\lambda_{eff}$ for H25 concrete taken from the ASTM standard [56]. Parameters $a$ and $b$ in sorption isotherm equation have taken from the paper [24].

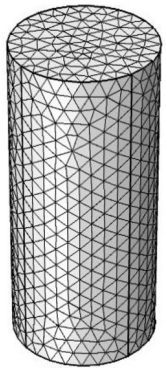

**Figure 9.** Finite element mesh for cylinder specimen.

## 4. Results & discussion

Cylinder specimens are modeled to simulate creep as well as drying phenomena and validated with the measured experimental results. The specifications of the specimens were described in the section 2. The specimens behavior modeled as 3D problem, and a mesh with tetrahedral elements used for space discretization. The material properties and parameters used in the model for all the concretes is shown in Table 7. Figure 9 shows the mesh of cylinder specimen to model creep. From the present experimental work, four concretes namely, M45, F45, SCC70 and H25 are selected to validate the present model. These concretes cover effects of different

 https://doi.org/10.1016/j.heliyon.2018.e00698

**Table 8.** Initial conditions for creep test.

| Variable | Value |
|---|---|
| $p_g$ | 101325 [Pa] |
| $p_c$ | RH = 98% |
| $T$ | 298.15 [K] |
| $\mathbf{u}$ | 0 |
| $\alpha_0$ | 0.05 |

**Table 9.** Boundary conditions for cylinder specimen for creep test.

| Side | Variable | Value up to 24 hrs of time | Value after 24 hrs of time |
|---|---|---|---|
| Top | $p_c$ | $q_c = 0$ | $q_c = 0$ |
| | $T$ | $q_T = 0$ | $q_T = 0$ |
| | $\mathbf{u}$ | $\mathbf{u} = 0$ | $\bar{\mathbf{t}}$ = 30% of $f_c$ at 14 or 28 days |
| Bottom | $p_c$ | $q_c = 0$ | $q_c = 0$ |
| | $T$ | $q_T = 0$ | $q_T = 0$ |
| | $\mathbf{u}$ | $\mathbf{u} = 0$ | $\mathbf{u} = 0$ |
| Radial side | $p_c$ | $q_c = 0$ | RH = 60% or 70% and $\beta_c = 0.002$ [m/s] |
| | $T$ | $q_T = 0$ | T = 298.15 [K] and $\alpha_c = 5$ [W m$^{-2}$ K] |

mineral admixtures (fly ash and silica fume) and aggregates (granite and hematite). The remaining concretes also contain the same mineral admixtures and aggregates hence these results are not shown in this study. In the simulations, to fix permeability coefficient experimental water loss data has been used.

## 4.1. Creep of M45 concrete

The material properties and parameters of M45 concrete used to model creep strain is given in the Table 7. This concrete was dried at the controlled environment of 70% RH and with the temperature at 25 °C and loaded at 14 days. The details of initial and boundary conditions used in the simulations are given in the Tables 8 and 9 respectively.

Figure 10 describes the evolution of the degree of hydration over the period of 1000 hrs. Figure 10 shows a higher progression of hydration degree in the initial 24 hrs period, because of the temperature rise due to sealed conditions during this period. The ultimate degree of cement hydration ($\alpha_u$) is estimated from the hydration model as 0.89.

Figure 11 shows the comparison between numerical and experimental results of water loss data of M45 concrete. The simulation results show overall a good agreement with experimental results. Figure 11 indicates a higher water loss during the early age, this is because of a rapid drying takes place due to high level of free water available in the concrete. Figure 12 shows the variation of humidity from day 1 to 200 days at the center point of the specimen. From the Figure 12 one

 https://doi.org/10.1016/j.heliyon.2018.e00698

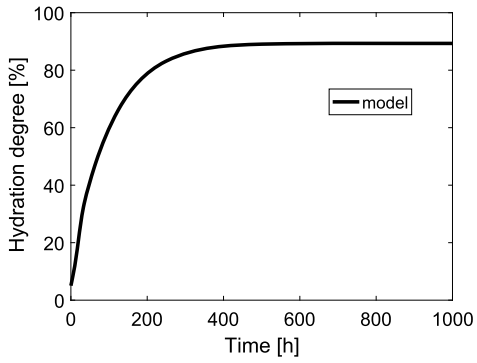


**Figure 10.** Simulated results of hydration degree for M45 concrete at mid point of inside the specimen.

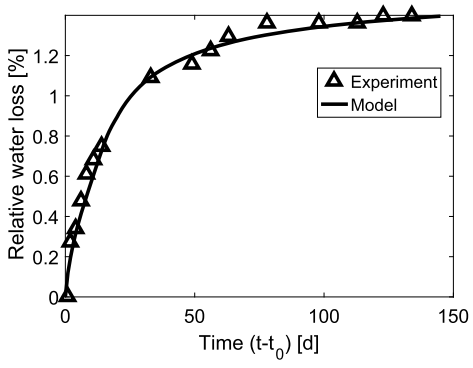


**Figure 11.** Comparison of measured and simulated relative mass loss data with time for M45 concrete, cured at 70% RH and 25 °C temperature.

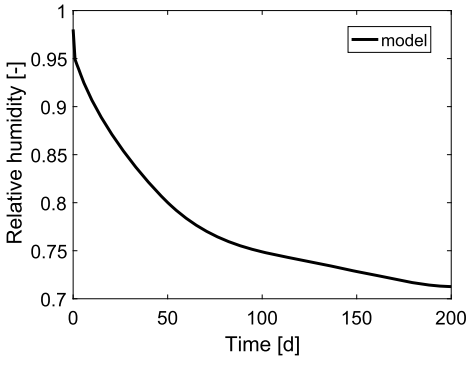


**Figure 12.** Simulated relative humidity (RH) M45 concrete at mid point of inside the specimen (cured at 70% RH and 25 °C).

can observe a rapid decrease in RH during the period of sealed condition, this is because of self desiccation phenomena. The model also captures the self desiccation phenomena during the hydration. Figure 13 shows the variation of temperature during the hydration up to 72 hrs. A maximum temperature of 339 K is observed during the first 24 hrs of time under sealed conditions there after one can see a rapid decrease in temperature. This is due to exchange of heat with the environment.

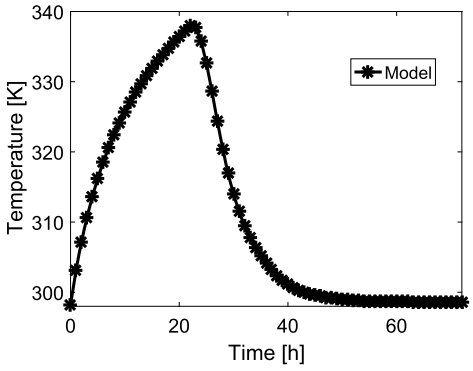


**Figure 13.** Simulated temperature with time for M45 concrete during hydration at mid point inside the specimen.

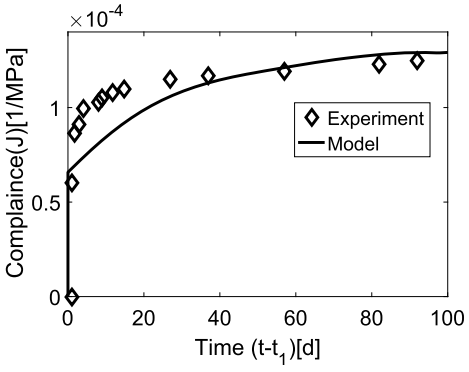


**Figure 14.** Comparison of measured and simulated total complaince for M45 concrete loaded at 14 days (dried at 70% RH and 25 °C temperature).

Figure 14 shows the comparison of simulated and experimental results of total compliance for M45 concrete loaded at 14 days. The simulated results show a good agreement with the experimental results.

## 4.2. Modeling of creep for F45 concrete

The material properties and parameters of F45 concrete used to model creep strain is given in the Table 7. This concrete dried at controlled environment of 60% RH and with the temperature at 25 °C and loaded at 14 days. The details of initial and boundary conditions used in the simulations are given in the Tables 8 and 9 respectively.

Figure 15 describes the evolution of degree of hydration with time. This figure shows a higher progression of hydration degree at initial 24 hrs period, which because of the temperature rise due to sealed conditions during this period. The ultimate degree of blended cement hydration is estimated from the hydration model as 0.91.

 https://doi.org/10.1016/j.heliyon.2018.e00698

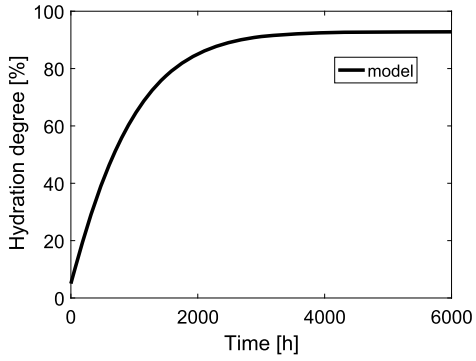


**Figure 15.** Simulated results of hydration degree for F45 concrete at mid point of inside the specimen.

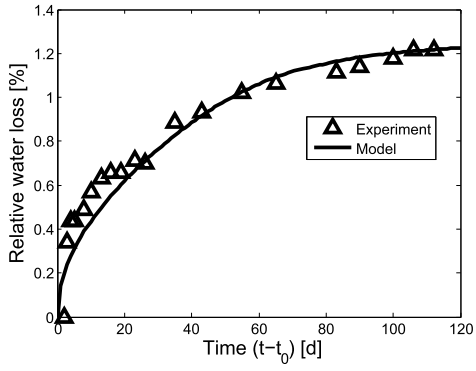


**Figure 16.** Comparison of measured and simulated relative water loss data with time for F45 concrete.

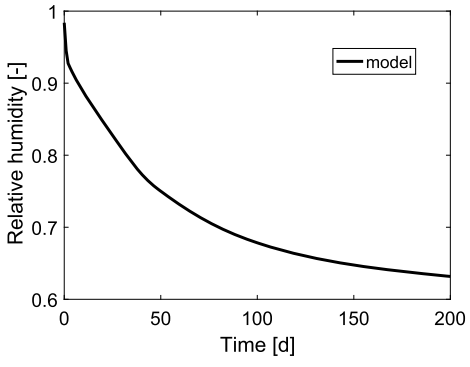


**Figure 17.** Simulated relative humidity (RH) F45 concrete at mid point of inside the specimen (cured at 60% RH and 25 °C).

Figure 16 shows the comparison between numerical and experimental results of water loss data of F45 concrete. The sorption isotherm given by Baroghel-Bounya et al. [24] is used to model the water loss. The simulation results shows overall a good agreement with the experimental results. Figure 17 shows the variation of humidity from day 1 to 200 days at center point of the specimen. From Figure 17, one can observe a rapid decrease in RH during the period of sealed condition, this

 https://doi.org/10.1016/j.heliyon.2018.e00698

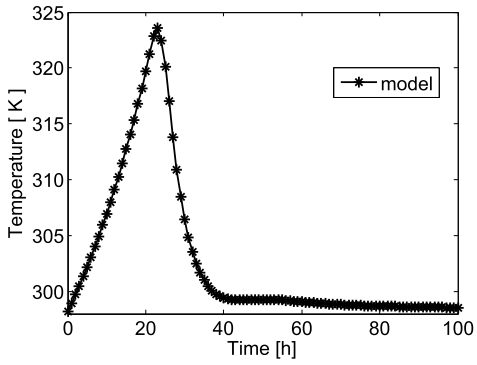


**Figure 18.** Simulated temperature with time for F45 concrete during hydration at mid point inside the specimen.

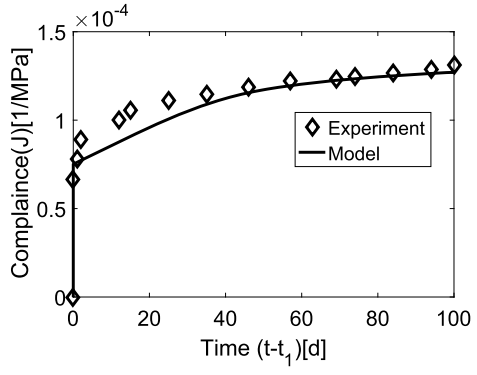


**Figure 19.** Comparison of measured and simulated total complaince for F45 concrete loaded at 14 days.

is because of self desiccation phenomena. The model has the ability to capture the self desiccation phenomena during the hydration. Figure 18 shows the variation of temperature during the hydration up to 72 hrs. A maximum temperature of 324 K is observed during the first 24 hrs of time under sealed conditions there after one can see a rapid decrease in temperature. This is due to exchange of heat with the environment. The rise in temperature is less when compared to the M45 concrete, this is because of the presence of fly ash. The fly ash reacts slowly and intern slows the production of heat.

Figure 19 shows the comparison of simulated and experimental results of total compliance for F45 concrete loaded at 14 days. The simulated results show a good agreement with the experimental results.

## 4.3. Modeling of creep for H25 concrete

The material properties and parameters for H25 concrete is used to model creep strain is given in the Table 7. This concrete dried at a controlled environment of

 https://doi.org/10.1016/j.heliyon.2018.e00698

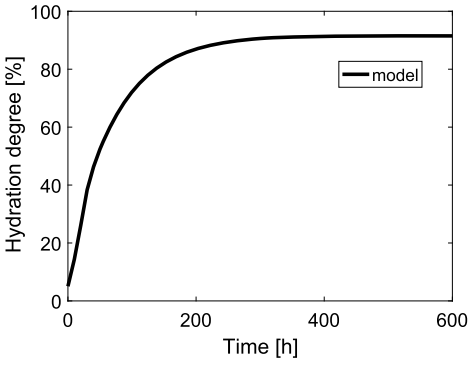


**Figure 20.** Simulation of hydration degree for H25 concrete at center point of the specimen.

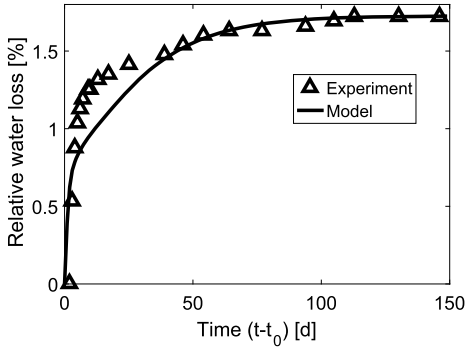


**Figure 21.** Comparison of measured and simulated relative water loss data with time for H25 concrete.

70% RH and with the temperature at 25 °C and loaded at 28 days. Since this is a special concrete, the material properties like heat capacity, thermal conductivity, etc are different from the normal concrete. These properties are calibrated based on the data available from the literature ([56,57,58]). The details of initial and boundary conditions used in the simulations are given in the Tables 8 and 9 respectively.

Figure 20 shows the evolution of degree of hydration with the time for H25 concrete. This figure shows a higher progression of hydration degree at initial 24 hrs period, which because of the temperature rise, due to sealed conditions during this period. The ultimate degree of cement hydration ($\alpha_u$) is estimated from the hydration model as 0.91.

Figure 21 shows the comparison between numerical and experimental results of water loss data for H25 concrete. The simulation results show overall a good agreement with experimental results. Figure 21 indicates a higher water loss at initial time, this is because of a rapid drying due to high level of free water available in the concrete. Figure 22 shows the variation of humidity from day 1 to 200 days at center point of the specimen.

 https://doi.org/10.1016/j.heliyon.2018.e00698

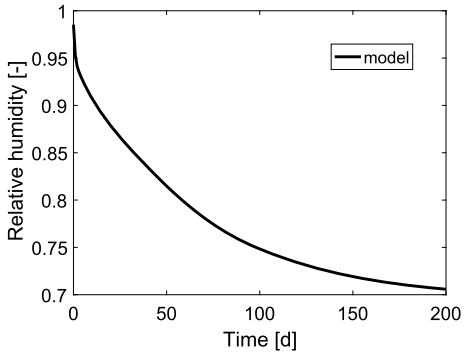


**Figure 22.** Simulated relative humidity (RH) H25 concrete at mid point of inside the specimen.

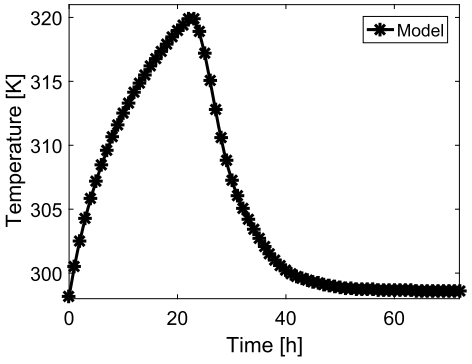


**Figure 23.** Simulated temperature with time for H25 concrete during hydration at mid point inside the specimen.

Figure 23 shows the variation of temperature during the hydration up to 72 hrs. A maximum temperature of 321 K is observed during the first 24 hrs of time under sealed conditions there after one can see a rapid decrease in temperature. This is due to exchange of heat with the environment. This concrete shows, the peak temperature is less than the other concretes. This is because of, the heat capacity of the hematite ore concrete is higher than the normal concrete. Figure 24 shows the comparison of simulated and experimental results of total compliance for H25 concrete loaded at 28 days. The simulated results show a good agreement with the experimental results.

## 4.4. Modeling of creep for SCC70 concrete

The material properties and parameters of SCC70 concrete used to model creep strain is given in Table 7. This concrete is dried in controlled environment at 60% RH and with the temperature at 25 °C, and is loaded at 14 days. The details of initial and boundary conditions used in the simulations are given in Tables 8 and 9 respectively.

Figure 25 describes the evolution of degree of hydration with time. This figure shows a higher progression of hydration degree at initial 24 hrs period, this is because of the

 https://doi.org/10.1016/j.heliyon.2018.e00698

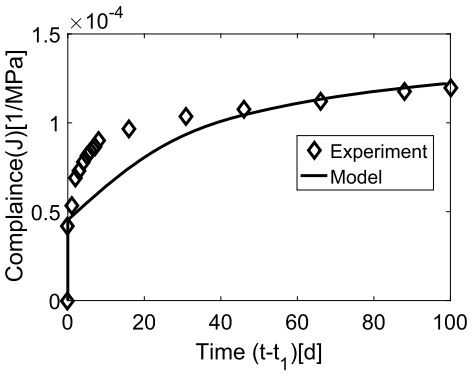


**Figure 24.** Comparison of measured and simulated total complaince for H25 concrete loaded at 28 days (dried at 70% RH and 25 °C temperature).

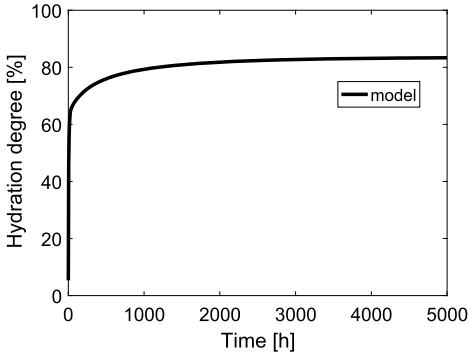


**Figure 25.** Simulated results of hydration degree for SCC70 concrete at mid point of inside the specimen.

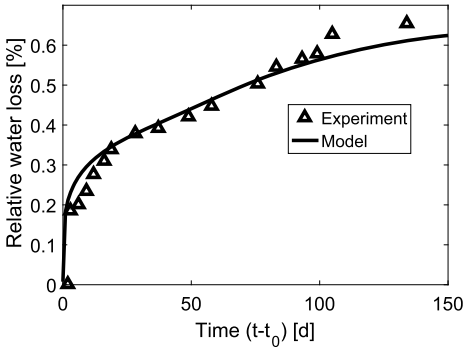


**Figure 26.** Comparison of measured and simulated relative water loss data with time for SCC70 concrete.

temperature rise is higher due to sealed conditions. The ultimate degree of blended cement hydration is estimated from the hydration model as 0.89. The fly ash and silica fume effects are considered while estimating the hydration degree. The total hydration of SCC70 concrete is calculated based on its mineral admixture fractions.

Figure 26 shows the comparison between numerical and experimental results of water loss data of SCC70 concrete. The x-axis shows drying time in days where

 https://doi.org/10.1016/j.heliyon.2018.e00698

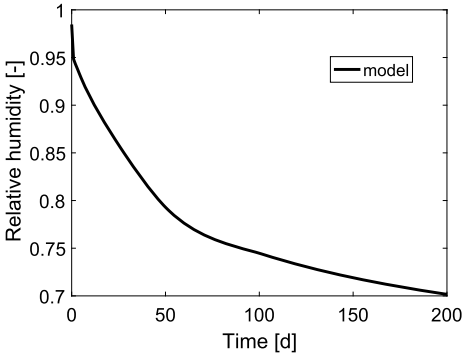


**Figure 27.** Simulated relative humidity (RH) SCC70 concrete at mid point of inside the specimen (cured at 60% RH and 25 °C).

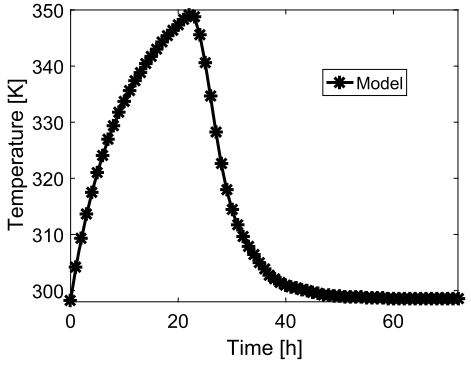


**Figure 28.** Simulated temperature with time for SCC70 concrete during hydration at mid point inside the specimen.

as y-axis shows the relative water loss. The sorption isotherm given by the Bounya et al. [24] is used to model the water loss. The simulation results shows overall a good agreement with experimental results. Figure 27 shows the variation of humidity from day 1 to 200 days at center point of the specimen. The simulated RH at 200 days is 70% but the environmental RH is 60%. This indicates the specimen RH has not reached equilibrium with environmental RH due to its slow drying process. This slower drying is because of its lower permeability coefficient when compared to the other concretes. Figure 28 shows the variation of temperature during the hydration up to 72 hrs. A maximum temperature of 350 K is observed during the first 24 hrs of time under sealed conditions there after a steep decrease in temperature is observed. This is due to exchange of heat with the environment. The rise in temperature is higher when compared to any other concretes, this is because of the presence higher cement and silica fume in the mix. The silica fume reacts rapidly and produces a higher heat than the cement.

 https://doi.org/10.1016/j.heliyon.2018.e00698

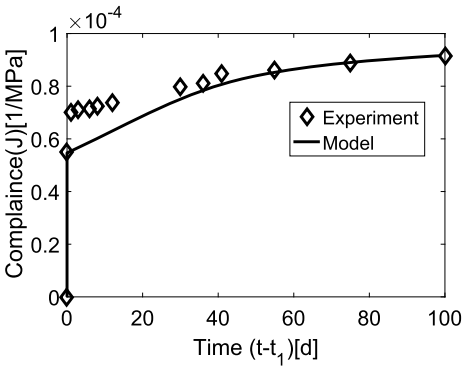


**Figure 29.** Comparison of measured and simulated total complaince for SCC70 concrete loaded at 14 days.

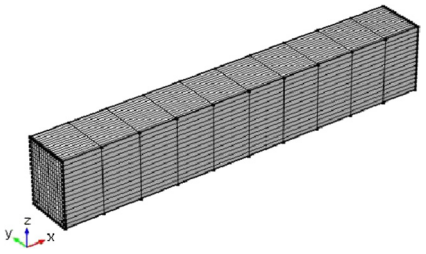


**Figure 30.** FEM mesh for the RCC beam.

Figure 29 shows the comparison of simulated and experimental results of total compliance for SCC70 concrete loaded at 14 days. The simulated results show a good agreement with the experimental results.

## 4.5. Modeling of creep for a benchmark problem

For validation of the above said model, a RCC beam studied for creep is selected [59]. In this study [59], the beam is cast and cured till 28 days and then a cracking load is applied and measured the deflection. This cracking load is sustained to measure time dependent deflection. The experiment was continued to till 380 days from the time of loading and deflection was measured. The FEM mesh for the beam and cross sectional and reinforcement details (2 nos 10 mm bars at bottom, 2 nos 6 mm bars at top and 6 mm stirrups at 100 mm intervals were used) as shown in the Figures 30 and 31 respectively. For discretizing the beam domain, a 8 node brick elements were used for concrete and 2 node link elements were used for reinforcement. The biaxial compressive strength of the concrete is taken as 1.2 times of the uni-axial compressive strength.

The detail of the material properties that has been used in the analysis is summarized in the Table 10,. For the boundary conditions, the study has not provided the

 https://doi.org/10.1016/j.heliyon.2018.e00698

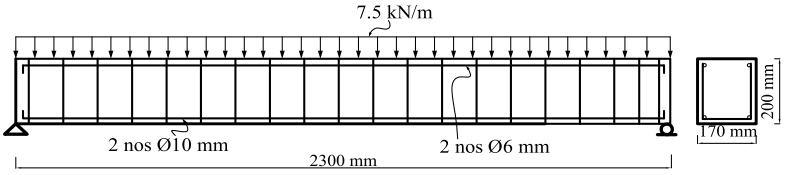


**Figure 31.** Details of the RCC beam.

**Table 10.** Properties of concrete and steel used in the model.

| Parameter | Symbol | Unit | Value |
|---|---|---|---|
| | Concrete | | |
| Porosity | $n$ | [%] | 12 |
| Cement | $c$ | [kg/m$^3$] | 331 |
| Water to cement ratio | $w/c$ | [-] | 0.45 |
| Aggregate to cement ratio | $w/c$ | [-] | 5.1 |
| Blaine | $Blaine$ | [m$^2$/kg] | 372 |
| Permeability | $k$ | [m$^2$] | $1 \times 10^{-18}$ |
| Activation energy | $E_a$ | [J/mol] | 46029 |
| Heat of hydration | $L_{hydr}$ | [J/g] | 472.9 |
| Ultimate hydration | $\alpha_u$ | [-] | 0.9 |
| parameter $A_0^c$ in equation (45) | $A_0^c$ | [-] | 0.0122 |
| Parameter $k_1$ in equation (44) | $k_1$ | [h] | 0.53 |
| Parameter $a$ in equation (32) | $a$ | [-] | 18.6237 |
| Parameter $b$ in equation (32) | $b$ | [-] | 2.2748 |
| Density | $\rho$ | [kg/m$^3$] | 2178 |
| Thermal conductivity | $\lambda_{eff}$ | [W/(m K)] | 1.7 |
| Specific Heat | $(C_p)_{eff}$ | [J/(kg K)] | 1020 |
| Elastic modulus | $E_c$ | [GPa] | 26.25 |
| Poisson's ratio | $\nu$ | [-] | 0.20 |
| Compressive strength | $f_c$ | [MPa] | 31.61 |
| Viscous parameter | $\mu_s$ | [1/(Pa*s)] | $1.44 \times 10^{-9}$ |
| Shrinkage coefficient | $k_{sh}$ | [-] | $6.82 \times 10^{-4}$ |
| | Steel | | |
| Elastic modulus | $E_s$ | [GPa] | 203.07 |
| Yield stress | $f_s$ | [MPa] | 413.56 |

casting details. Hence in the analysis, the first 7 days is assumed to be a sealed boundary conditions for all the sides except top longitudinal side. After 7 days, the environmental humidity and temperature reported in the study is specified on the boundaries. The initial conditions are specified in the Table 8 and the boundary conditions used in the simulation is as shown in the Table 11. The Willam and Warnke yield criterion [54] is used to capture an extra yield surface due to plasticity. The cracking effects is considered through the smeared crack model [60] while modeling the beam.

Figure 32 shows the simulated degree of hydration at center point of the beam. In this figure x-axis shows the time in hours and the y-axis shows the hydration degree. The hydration degree at 5000 hrs from the time of casting is about 0.89.

Figure 33 shows the simulated relative humidity at center point of the beam. From Figure 33, one can observe a light decrease in RH from day 2 to day 7, this is because,

 https://doi.org/10.1016/j.heliyon.2018.e00698

**Table 11.** Boundary conditions of the beam.

| Side | Variable | Value up to 7 days | Value after 7 days |
|---|---|---|---|
| | | For $p_c$ and $T$ | |
| All sides (except top side) | $p_c$ | $q_c = 0$ | RH = 60% and $\beta_c = 0.002$ [m/s] |
| | $T$ | $q_T = 0$ | T = 298.15 [K] and $\alpha_c = 8$ [W m$^{-2}$ K] |
| Top side | $p_c$ | RH = 60% and $\beta_c = 0.002$ [m/s] | RH = 60% and $\beta_c = 0.002$ [m/s] |
| | $T$ | T = 298.15 [K] and $\alpha_c = 8$ [W m$^{-2}$ K] | T = 298.15 [K] and $\alpha_c = 8$ [W m$^{-2}$ K] |
| | | For $u$ | |
| Left bottom edge | $u$ | – | $u_x, u_y, u_z = 0$ |
| Right bottom edge | $u$ | – | $u_z, u_y = 0$ |
| Top side | $u$ | – | $\bar{t} = 7.5$ kN/m, applied at 28 days |

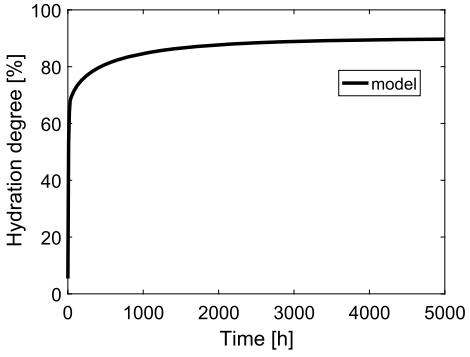


**Figure 32.** Simulated hydration degree for RCC beam.

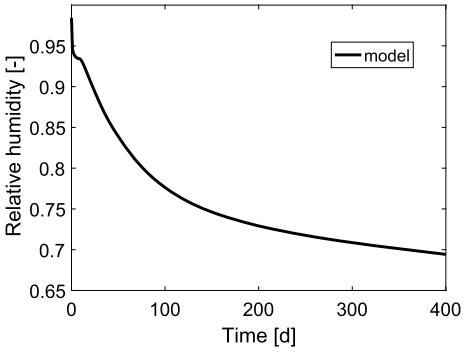


**Figure 33.** Simulated relative humidity for RCC beam.

the self dessication is high during first day because of rapid hydration, there after the self dessication is slow hence reduction in RH also slows. And also this figure shows that the value of RH is about 71% at 400 days from the time casting and the environmental humidity is 60% RH, this indicates the beam is not reached to the equilibrium.

 https://doi.org/10.1016/j.heliyon.2018.e00698

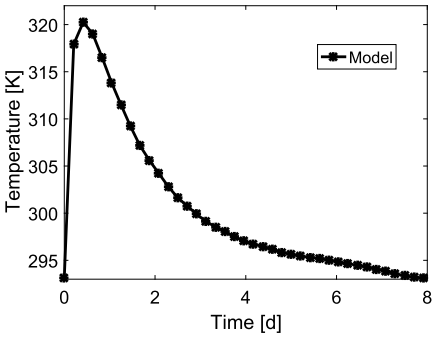


**Figure 34.** Simulated temperature for RCC beam at center point from bottom of the RCC beam.

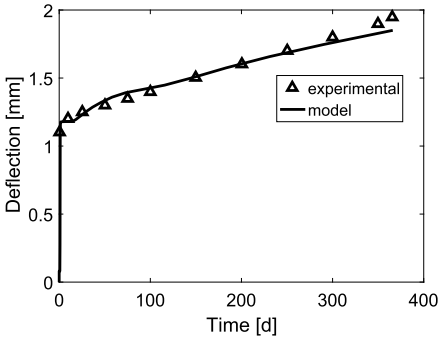


**Figure 35.** Comparison of experimental and simulated results for total deflection of the RCC beam.

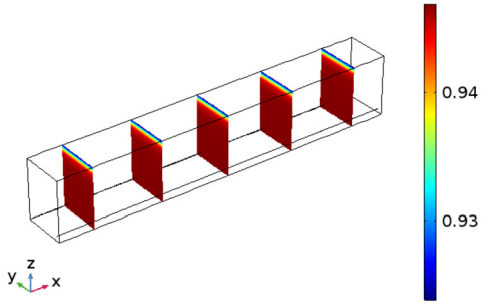


**Figure 36.** Simulated RH of the beam at 23 hrs.

Figure 34 shows the variation of temperature during the hydration up to 72 hrs. A maximum temperature of 320 K is observed during the first 24 hrs of time under indicated boundary conditions (11) there after a gradual decrease in temperature is observed till seven days and there after the beam is achieved an equilibrium condition.

Figure 35 shows the comparison of measured deflection with simulated deflection results. The model shows a good agreement with experimental values.

Figures 36 and 37 shows the simulated results of relative humidity gradients at 23 hrs and 200 days. Figure 36 shows a rapid decrease in humidity from initial condition

 https://doi.org/10.1016/j.heliyon.2018.e00698

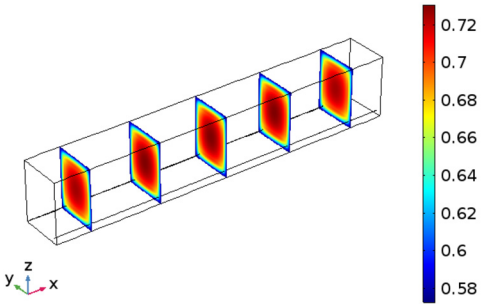


**Figure 37.** Simulated RH of the beam at 200 days.

98% to 94% at 23 hrs, this is due to the self dessication of cement hydration. Figure 37 shows the gradual drying of concrete. Where the relative humidity decreased from 94% to 72% at center of the specimen.

## 5. Conclusions

This study investigates the effects of mineral admixtures as well as type of aggregate on drying and creep properties of concrete through an experimental and analytical study. Based on experimental and analytical results the following conclusions can be drawn.

- H25 concrete shows a higher creep strain than any of the other concretes due to the lower water absorption coefficient of hematite aggregate.
- The F45 concrete showing higher compressive strength over the age due to its prolonged hydration. The F45 concrete shows lower creep strain than the normal M45 concrete. The high volume fly ash concretes shows a prolonged hydration and this increases the stiffness over the time. This increase in stiffness reduces the creep strain.
- SCC35 concrete shows a higher creep than the other SCC concretes. This difference comes from the aggregate to cement ratio (a/c), higher the aggregate to cement ratio, lower the creep. M35 concrete has higher a/c than the other SCC concretes.
- SCC70 concrete shows a lower creep than any other concrete throughout the drying period. This is due to its lower permeability and this delays the rate of drying and reduces the drying creep.
- Fly ash concretes shows a lesser creep than OPC concretes.
- The governing equations of the model are developed based on a poromechanics approach. The state variables of the model is capillary pressure $p_c$, temperature $T$, and displacements $u$. The internal variable of the model are the degree of hydration $\alpha$. The effects of mineral admixtures, like fly ash and silica fume, are considered while estimating the degree of hydration. The material

 https://doi.org/10.1016/j.heliyon.2018.e00698

properties of concrete, like porosity, compressive strength, elastic modulus, etc. are treated as a function of the degree of hydration.

- The micro prestress solidification theory is used in conjunction with estimates of $p_c$ and $T$ to validate creep of concrete. This model is validated with the available reported data and with experimental data from the present study. The model accurately predicts the temperature and relative humidity (RH) gradients of the concrete during the hydration and beyond. This helps to predict long term deformation like creep accurately. The temperature and RH are the main parameters for most of the creep prediction models. The present is able to predict the creep strains and water loss data (drying phenomenon) for all the different concrete types having different strengths and curing conditions very well indicating the robustness of the model.
- The model has predicted results for creep strains at mid point in a reinforced concrete beam under sustained loads and varying environmental conditions with good agreement indicating its robustness.

## Declarations

## Author contribution statement

D. Harinadha Reddy: Performed the experiments; Analyzed and interpreted the data; Contributed reagents, materials, analysis tools or data; Wrote the paper.

Ananth Ramaswamy: Conceived and designed the experiments; Contributed reagents, materials, analysis tools or data; Wrote the paper.

## Competing interest statement

The authors declare no conflict of interest.

## Funding statement

This work was supported by the Board of research in Nuclear Science, Government of India through grant Number 2012/36/42 BRNS 12-10-2012.

## Additional information

No additional information is available for this paper.

 https://doi.org/10.1016/j.heliyon.2018.e00698

## References

[1] K. Kovler, Drying creep of concrete in terms of the age-adjusted effective modulus method, Mag. Concr. Res. 49 (181) (1997) 345–352.

[2] D. Gawin, F. Pesavento, B.A. Schrefler, Hygro-thermo-chemo-mechanical modelling of concrete at early ages and beyond. Part I: hydration and hygro-thermal phenomena, Int. J. Numer. Methods Eng. 67 (3) (2006) 299–331.

[3] M. Cervera, J. Oliver, T. Prato, Thermo-chemo-mechanical model for concrete. I: hydration and aging, J. Eng. Mech. 125 (9) (1999) 1018–1027.

[4] D. Gawin, F. Pesavento, B.A. Schrefler, Hygro-thermo-chemo-mechanical modelling of concrete at early ages and beyond. Part II: shrinkage and creep of concrete, Int. J. Numer. Methods Eng. 67 (3) (2006) 332–363.

[5] A. Ross, Some problems in concrete construction, Mag. Concr. Res. 12 (34) (1960) 27–34.

[6] P. Bamforth, In situ measurement of the effect of partial Portland cement replacement using either fly ash or ground granulated blast-furnace slag on the performance of mass concrete, Proc., Inst. Civ. Eng. 69 (3) (1980) 777–800.

[7] R. Lohtia, B. Nautiyal, O. Jain, Creep of fly ash concrete, ACI J. 73 (39) (1976) 469–472.

[8] M. Buil, P. Acker, Creep of a silica fume concrete, Cem. Concr. Res. 15 (3) (1985) 463–466.

[9] R. Khatri, V. Sirivivatnanon, W. Gross, Effect of different supplementary cementitious materials on mechanical properties of high performance concrete, Cem. Concr. Res. 25 (1) (1995) 209–220.

[10] M. Mazloom, A. Ramezanianpour, J. Brooks, Effect of silica fume on mechanical properties of high-strength concrete, Cem. Concr. Compos. 26 (4) (2004) 347–357.

[11] R.S. Ghosh, J. Timusk, Creep of fly ash concrete, J. Proc. 78 (1981) 351–357.

[12] M. Collepardi, S. Collepardi, R. Troli, Properties of scc and flowing concrete, in: Proceedings of the International Conference of Sustainable Construction Materials and Technologies, Coventry: Pub. UW Milwaukee CBU, 2007, pp. 25–31.

[13] S.A. Kristiawan, A.P. Nugroho, Creep behaviour of self-compacting concrete incorporating high volume fly ash and its effect on the long-term deflection of reinforced concrete beam, Proc. Eng. 171 (2017) 715–724.

 https://doi.org/10.1016/j.heliyon.2018.e00698

[14] H.H. Alghazali, J.J. Myers, Creep and shrinkage of ecological self consolidating concrete, in: International Conference on Performance-Based and Life-Cycle Structural Engineering, School of Civil Engineering, The University of Queensland, 2015, pp. 1619–1627.

[15] IS383, Specification for coarse and fine aggregate from natural sources for concrete, Indian Standard Institution New Delhi, Beauro of Indian Standards.

[16] IS12269, Specifications for 53 grade ordinary Portland cement, Indian Standard Institution New Delhi, Beauro of Indian Standards.

[17] ASTM C618, Standard specification for coal fly ash and raw or calcined natural pozzolan for use in concrete, ASTM Standards, ASTM.

[18] www.fosroc com, Supplier of admixtures for concrete.

[19] ASTM C512/C512M, Standard test method for creep of concrete in compression, ASTM Standards, ASTM.

[20] O. Gencel, W. Brostow, C. Ozel, M. Filiz, Concretes containing hematite for use as shielding barriers, Materials Science (Medziagotyra) 16 (3) (2010).

[21] Z.P. Bazant (Ed.), Mathematical Modeling of Creep and Shrinkage of Concrete, Wiley Chichester, Wiley, 1988.

[22] O. Coussy, Poromechanics, John Wiley & Sons, 2004.

[23] M. Mainguy, O. Coussy, V. Baroghel Bouny, Role of air pressure in weakly permeable materials, J. Eng. Mech. 127 (2001) 582–592.

[24] V. Baroghel-Bounya, M. Mainguya, T. Lassabatereb, O. Coussy, Characterization and identification of equilibrium and transfer moisture properties for ordinary and high-performance cementitious materials, Cem. Concr. Res. 29 (1999) 1225–1238.

[25] M. Hassanizadeh, W.G. Gray, General conservation equations for multi-phase systems: 1. Averaging procedure, Adv. Water Resour. 2 (1979) 131–144.

[26] W.G. Gray, S. Hassanizadeh, Averaging theorems and averaged equations for transport of interface properties in multiphase systems, Int. J. Multiph. Flow 15 (1) (1989) 81–95.

[27] S.J. Gregg, K.S.W. Sing, H. Salzberg, Adsorption surface area and porosity, J. Electrochem. Soc. 114 (11) (1967) 279C.

[28] R.W. Lewis, B.A. Schrefler, The Finite Element Method in the Static and Dynamic Deformation and Consolidation of Porous Media, John Wiley, 1998.

[29] R. Lewis, B. Schrefler, The finite element method in the static and dynamic deformation and consolidation of porous media, Meccanica 34 (3) (1999) 231–232.

[30] Y. Xi, Z.P. Bažant, H.M. Jennings, Moisture diffusion in cementitious materials adsorption isotherms, Adv. Cem. Based Mater. 1 (6) (1994) 248–257.

[31] S. Poyet, Experimental investigation of the effect of temperature on the first desorption isotherm of concrete, Cem. Concr. Res. 39 (11) (2009) 1052–1059.

[32] K.K. Hansen, Sorption Isotherms: A Catalogue, Ph.D. thesis, Technical University of Denmark, Danmarks Tekniske Universitet, Department of Structural Engineering and Materials, Institut for Bærende Konstruktioner og Materialer, 1986.

[33] A. Feraille-Fresnet, P. Tamagny, A. Ehrlacher, J. Sercombe, Thermo-hydro-chemical modelling of a porous medium submitted to high temperature: an application to an axisymmetrical structure, Math. Comput. Model. 37 (5) (2003) 641–650.

[34] D.J. Furbish, Fluid Physics in Geology: An Introduction to Fluid Motions on Earth's Surface and Within Its Crust, Oxford University Press, Oxford, 1997.

[35] ASTM C642, Standard Test Method for Density, Absorption, and Voids in Hardened Concrete, Annual book of ASTM standards, 2006.

[36] D. Gawin, C. Majorana, B. Schrefler, Numerical analysis of hygro-thermal behaviour and damage of concrete at high temperature, Mech. Cohes.-Frict. Mater. 4 (1) (1999) 37–74.

[37] R.C. Reid, J.M. Prausnitz, B.E. Poling, The Properties of Gases and Liquids, McGraw Hill Book Co., New York, NY, 1987.

[38] F. Lin, Christian Meyer, Modelling of thermochemomechanical couplings of concrete at early ages modeling of Portland cement considering the effects of curing temperature and applied pressure, Cem. Concr. Res. 39 (2009) 255–265.

[39] F.-J. Ulm, O. Coussy, Modeling of thermochemomechanical couplings of concrete at early ages, J. Eng. Mech. 121 (7) (1995) 785–794.

[40] T.C. Powers, T.L. Brownyard, Studies of the physical properties of hardened Portland cement paste, J. Proc. 43 (1946).

[41] A.K. Schindler, Effect of temperature on hydration of cementitious materials, ACI Mater. J. 101 (1) (2004).

[42] F. Lin, C. Meyer, Hydration kinetics modeling of Portland cement considering the effects of curing temperature and applied pressure, Cem. Concr. Res. 39 (4) (2009) 255–265.

 https://doi.org/10.1016/j.heliyon.2018.e00698

[43] G. Di Luzio, G. Cusatis, Hygro-thermo-chemical modeling of high performance concrete. I: Theory, Cem. Concr. Compos. 31 (5) (2009) 301–308.

[44] J. Yajun, J. Cahyadi, Simulation of silica fume blended cement hydration, Mater. Struct. 37 (6) (2004) 397–404.

[45] R.H. Bogue, The Chemistry of Portland Cement, Reinhold Publishing Corporation, 1947.

[46] V. Waller, F. De Larrard, P. Roussel, et al., Modelling the temperature rise in massive hpc structures, in: 4th International Symposium on Utilization of High-Strength/High-Performance Concrete, 1996, pp. 415–421.

[47] R. Mills, Factors Influencing Cessation of Hydration in Water Cured Cement Pastes, Highway Research Board special report, 1996.

[48] L.E. Copeland, D. Kantro, G.J. Verbeck, Chemistry of Hydration of Portland Cement, 1960, Citeseer.

[49] J.F. Young, W. Hansen, Volume Relationships for C–S–H Formation Based on Hydration Stoichiometries, MRS Proc., vol. 85, Cambridge Univ. Press, 1986, p. 313.

[50] K. Maekawa, T. Ishida, T. Kishi, Multi-Scale Modeling of Structural Concrete, CRC Press, 2008.

[51] Z.P. Bazant, S. Prasannan, Solidification theory for concrete creep. I: formulation, J. Eng. Mech. 115 (8) (1989) 1691–1703.

[52] Z.P. Bazant, S. Prasannan, Solidification theory for concrete creep. II: verification and application, J. Eng. Mech. 115 (8) (1989) 1704–1725.

[53] Z.P. Bazant, Y. Xi, Continuous retardation spectrum for solidification theory of concrete creep, J. Eng. Mech. 121 (2) (1995) 281–288.

[54] K. Willam, E. Warnke, Constitutive model for the triaxial behavior of concrete, in: Proceedings, International Association for Bridge and Structural Engineering, vol. 19, ISMES, Bergamo, Italy, 1975, pp. 1–30.

[55] K. Maekawa, R. Chaube, T. Kishi, Modeling of Concrete Performance: Hydration, Microstructure Formation and Mass Transport, E and FN SPON, London, 1999.

[56] J.F. Lamond, J.H. Pielert, Significance of Tests and Properties of Concrete and Concrete-Making Materials, ASTM, West Conshohocken, PA, 2006.

[57] W.H. Johnson, W.H. Parsons, Thermal Expansion of Concrete Aggregate Materials, US Government Printing Office, 1944.

[58] V. Rao, Thermal conductivity and diffusivity of iron ore pellet having low porosity, ISIJ Int. 42 (7) (2002) 800–802.

[59] W.-C. Choi, H.-D. Yun, Long-term deflection and flexural behavior of reinforced concrete beams with recycled aggregate, Mater. Des. 51 (2013) 742–750.

[60] R. De Borst, P. Nauta, Non-orthogonal cracks in a smeared finite element model, Eng. Comput. 2 (1) (1985) 35–46.